

# Cardiovascular Parameter Estimation using a Computational Model

by  
Zaid Samar

Bachelor of Science in Electrical Engineering  
Georgia Institute of Technology, 2002

Submitted to the Department of Electrical Engineering and Computer  
Science

in partial fulfillment of the requirements for the degree of  
Master of Science in Electrical Engineering and Computer Science  
at the

MASSACHUSETTS INSTITUTE OF TECHNOLOGY

May 2005

© Massachusetts Institute of Technology 2005. All rights reserved.

Author .....  
Department of Electrical Engineering and Computer Science  
May 23, 2005

Certified by .....  
Roger G. Mark  
Distinguished Professor of Health Sciences and Technology  
Professor of Electrical Engineering  
Thesis Supervisor

Certified by .....  
George C. Verghese  
Professor of Electrical Engineering  
Thesis Supervisor

Certified by .....  
Thomas Heldt  
Postdoctoral Associate  
Lab for Electromagnetic & Electronic Systems  
Thesis Co-Supervisor

Accepted by .....  
Arthur C. Smith  
Chairman, Department Committee on Graduate Students

*To my parents, Yusuf and Nighat.*

# Cardiovascular Parameter Estimation using a Computational Model

by

Zaid Samar

Submitted to the Department of Electrical Engineering and Computer Science  
on May 23, 2005, in partial fulfillment of the  
requirements for the degree of  
Master of Science in Electrical Engineering and Computer Science

## Abstract

Modern intensive care units (ICU's) are equipped with a wide range of patient monitoring devices, each continuously recording signals produced by the human body. Currently, these signals need to be interpreted by a clinician in order to assess the state of the patient, to formulate physiological hypotheses, and to determine treatment options. With recent technological advances, the volume of relevant patient data acquired in a clinical setting has increased. This increase in sheer volume of data available, and its lack of organization, have rendered the clinical decision-making process inefficient. In some areas, such as hemodynamic monitoring, there is enough quantitative information available to formulate computational models capable of simulating normal and abnormal human physiology. Computational models can help to synthesize information in one common framework, thereby improving data integration and organization. Through tuning, such models could be used to track patient state automatically and to relate properties of the observable data streams directly to the properties of the underlying cardiovascular system.

In our research efforts, we implemented a pulsatile cardiovascular model and attempted to match its output to simulated observable hemodynamic signals collected in the ICU, in order to estimate cardiovascular parameters. Tracking model parameters in time reveals disease progression, and hence can be very useful for patient monitoring purposes. As the observable signals are generally not rich enough to allow for the estimation of all the model parameters, we focused on estimating only a subset of parameters.

Our simulations indicate that observable data at intra-beat timescales can be used to estimate distending blood volume, peripheral resistance, and end-diastolic right compliance to reasonable degrees of accuracy. Furthermore, our simulation results based on a real patient hemorrhage case reveal that clinically significant parameters related to bleeding rate and peripheral resistance can be tracked reasonably well using observable patient data at inter-beat timescales.

Thesis Supervisor: Roger G. Mark  
Title: Distinguished Professor of Health Sciences and Technology  
Professor of Electrical Engineering

Thesis Supervisor: George C. Verghese  
Title: Professor of Electrical Engineering

Thesis Co-Supervisor: Thomas Heldt  
Title: Postdoctoral Associate  
Lab for Electromagnetic & Electronic Systems

# Acknowledgments

I would like to thank Professor Roger Mark and Professor George Verghese for their guidance and support throughout my time at MIT. I am extremely fortunate to have been groomed under both of them, and I am in total awe of the keen insight with which they have guided me.

I would also like to thank Dr. Thomas Heldt who has been a source of inspiration and guidance, not only in matters related to research, but in all aspects of graduate student life in general. I am also grateful to him for his assistance during the writing of this thesis.

I am indebted to Tushar Parlikar and Carlos Renjifo for their support and encouragement throughout. Together, we were the first student members of the ‘modeling group’ and I have had a great time working with them. From our initial sporadic meetings in TA rooms to our weekly meetings in the LEES headquarters, we have come a long way and it has been a lot of fun.

A special thanks to all the members of the Laboratory for Computational Physiology who made my stay there an endearing one. I would like to thank Mohammed Saeed who introduced me to the group’s activities which subsequently captured my interest in this area of research. Mohammed also introduced me to the powerful domain of Simulink. I would like to thank Dr. Gari Clifford for all his help and support. I am also thankful to Gari for driving me to exercise in the form of playing squash with him (before my laziness got the better of me). I would like to thank James Sun, Tin Kyaw and Omar Abdala for their support and friendship. I am especially thankful to James Sun for his contributions towards our work. I am grateful to Dr. Brian Janz and Dr. Andrew Reisner for their expert medical insight which allowed us to move forward with our research goals.

I want to thank Adnan Dosani, whose friendship and support played important roles in my decision to join MIT. Throughout my undergraduate and graduate school experiences, Adnan has always been there to share my grievances and celebrate my moments of success and happiness.

I would like to thank Amil Haque, Usman Jameel, and Shinoj Shamsuddin for their

support, prayers, and good wishes. I have known these guys for more than a decade now and I am grateful that we are still very much in touch, despite the distances that separate us.

I thank Rehan Tahir, Zubair Anwar, and Faisal Kashif for their support and culinary skills. Their friendship, and the food which they fed me, have made my MIT experience a memorable one. Faisal also provided me with much needed company at odd hours of the night during the writing process, for which I am grateful. I would also like to thank Hasan Ansari for his friendship and support; his antics have always managed to bring a smile to my face. I am also grateful to Ebad Ahmed and Omair Malik for their encouragement.

Finally, I come to those who matter most. I would like to thank my sister, Maleeha, for her love and support. She has always been the elder sibling who has looked out for me at every stage. I would like to express my deepest gratitude to my parents, Yusuf and Nighat, for all the sacrifices they have made to provide me with the very best. Their love, support, and prayers have been the driving forces behind all my achievements.

This work was supported in part through the National Aeronautics and Space Administration (NASA) through the NASA Cooperative Agreement NCC 9-58 with the National Space Biomedical Research Institute and in part by Grant RO1 EB001659 from the National Institute of Biomedical Imaging and Bioengineering.

# Contents

<b>1</b>	<b>Introduction</b>	<b>17</b>
1.1	Motivation . . . . .	17
1.2	The Cardiovascular System . . . . .	19
1.3	Cardiovascular Models and Model-Based Reasoning . . . . .	20
1.4	Hemodynamic Monitoring in an ICU . . . . .	21
1.5	Thesis Goals and Outline . . . . .	23
<b>2</b>	<b>The Computational Hemodynamic Model</b>	<b>25</b>
2.1	Simplifying Assumptions . . . . .	26
2.2	CVSIM . . . . .	26
2.3	The Model Implementation . . . . .	28
2.3.1	The Platform . . . . .	28
2.3.2	Nominal Parameter Values . . . . .	28
2.3.3	The Time-Varying Compliance Function . . . . .	29
2.3.4	The Model Dynamics . . . . .	30
2.3.5	Initial Conditions . . . . .	32
2.3.6	Conservation of Volume . . . . .	33
2.3.7	Model Validation . . . . .	35
2.3.8	Interstitial Fluid Compartment . . . . .	36
2.3.9	Concluding Remarks . . . . .	40

<b>3</b>	<b>The Cardiovascular Control System</b>	<b>43</b>
3.1	Arterial Baroreflex . . . . .	44
3.2	Implementation . . . . .	44
3.2.1	Preprocessing and Error Calculation . . . . .	45
3.2.2	Effector Mechanism . . . . .	46
3.3	Qualitative Validation . . . . .	51
3.3.1	Hemorrhage . . . . .	51
3.3.2	Left Myocardial Infarction (MI) . . . . .	52
3.4	Concluding Remarks . . . . .	53
<b>4</b>	<b>Parameter Estimation using Waveform Data</b>	<b>55</b>
4.1	Nonlinear Least Squares and Subset Selection . . . . .	56
4.1.1	Nonlinear Least Squares Optimization . . . . .	56
4.1.2	Subset Selection . . . . .	58
4.1.3	Jacobian Calculation and Scaling . . . . .	60
4.1.4	Application of the Subset Selection Algorithm . . . . .	62
4.1.5	Description of the Estimation Problem . . . . .	63
4.2	Results . . . . .	63
4.2.1	Estimation using Steady-State Waveform Data . . . . .	63
4.2.2	Estimation using Transient Waveform Data (Hemorrhage Data) . . . . .	66
4.3	Concluding Remarks . . . . .	69
<b>5</b>	<b>Parameter Tracking using Beat-to-Beat Averaged Data</b>	<b>71</b>
5.1	Brief Patient History . . . . .	72
5.2	Patient Data for Parameter Tracking . . . . .	72
5.3	Simulating Patient Data . . . . .	74
5.4	Parameter Tracking . . . . .	77
5.5	Results . . . . .	80
5.6	Concluding Remarks . . . . .	81

<b>6</b>	<b>Conclusions and Recommendations for Future Work</b>	<b>83</b>
6.1	Summary . . . . .	83
6.2	Recommendations for Future Work . . . . .	85
<b>A</b>	<b>Updated CVSIM Model Equations</b>	<b>89</b>
<b>B</b>	<b>Independent Parameters of the CVSIM Model</b>	<b>93</b>
<b>C</b>	<b>Peripheral Resistance Estimation based on Patient Data</b>	<b>95</b>
C.1	Assumptions on Changes in Peripheral Resistance . . . . .	95
C.2	Peripheral Resistance Estimation using the Windkessel Model . . . . .	96
C.3	Concluding Remarks . . . . .	100



# List of Figures

1-1	The Circulation System [1]. . . . .	20
2-1	Circuit analog of the CVSIM model. . . . .	27
2-2	Ventricular compliance function and its derivative. . . . .	30
2-3	Difference between expected total blood volume ( $Q_{Total}$ ) and calculated total blood volume ( $\hat{Q}_{Total}$ ), with left and right ventricular pressure (voltage) as state variables. . . . .	34
2-4	Difference between expected total blood volume ( $Q_{Total}$ ) and calculated total blood volume ( $\hat{Q}_{Total}$ ), with left and right ventricular volume (charge) as state variables. . . . .	34
2-5	Pulsatile pressure waveforms for a single beat. . . . .	36
2-6	Volume distribution for an average 70-kg adult. Approximately 60% of body mass is fluid. This percentage can vary depending on age, sex, and obesity [2].	37
2-7	Addition of the interstitial compartment between the systemic arteries and veins. . . . .	39
2-8	Beat-to-beat averaged venous charge ( $Q_v^{av}$ ) vs time. Sub-figure (a) shows the plot of $Q_v^{av}$ vs time before and after the administration of a fluid bolus. Sub-figure (b) shows the plot of $\ln(Q_v^{av})$ vs time, and its best straight line fit, after the administration of a fluid bolus. The time-constant for the charge decay is the reciprocal of the slope of the best straight line fit: $\tau_{int} \approx 4.5$ min. . . . .	40
2-9	$Q_{incoming}^{av} - Q_{outgoing}^{av}$ after the administration of a fluid bolus. . . . .	41

3-1	Block diagram of the arterial baroreflex system. $P_a^{sp}$ is the set-point pressure that the system is aiming to maintain. . . . .	45
3-2	Block diagram depicting the preprocessing involved. . . . .	46
3-3	Impulse response and magnitude of Fourier transform of sympathetic and parasympathetic filters. The impulse responses are estimated from canine data [3]. . . . .	47
3-4	Diagrammatic representation of the effector mechanism depicting autonomic mediation. . . . .	48
3-5	Open-loop step responses of sympathetic and parasympathetic filters as implemented using Simulink. . . . .	50
3-6	Nominal parasympathetic impulse response and its Padé approximations. . .	51
3-7	Open-loop step response comparison of the nominal parasympathetic filter and its approximations. . . . .	52
3-8	Parasympathetic block output during hemorrhage and left MI simulations using different approximations for the parasympathetic filter. . . . .	53
3-9	Hemorrhage simulation. . . . .	54
3-10	Left MI simulation. . . . .	54
4-1	Eigenvalue spectrum of the Hessian approximation under the two different scaling schemes applied. . . . .	62
4-2	Estimated active parameters recovered using steady-state waveform data vs actual active parameters. . . . .	65
4-3	Estimated vs actual change in DBV for all the simulated hemorrhage cases analyzed. . . . .	67
4-4	Estimated vs actual $R_a$ for all the hemorrhage cases analyzed. . . . .	68
4-5	Estimated $C_r^{ed}$ vs actual $C_r^{ed}$ for the hemorrhage cases. . . . .	69
5-1	Heart rate (upper panel) and arterial blood pressure (lower panel) patient data.	73
5-2	Levophed administration (top panel) and beat-to-beat averaged patient ABP data (bottom panel). . . . .	74

5-3	Simulated beat-to-beat averaged ABP data (top panel) and actual patient ABP data (bottom panel). . . . .	76
5-4	Beat-to-beat averaged ABP data: actual and simulated with additive noise. . . . .	77
5-5	Simulated beat-to-beat averaged CVP data. . . . .	79
5-6	Diagram depicting the neglect of intra-beat dynamics under the proposed scheme to estimate initial conditions. . . . .	80
5-7	Plot showing portion of ABP data following a fluid bolus and its reconstructed version using exact parameters and estimated initial conditions using two different schemes. . . . .	81
5-8	Estimated versus actual parameters. . . . .	82
A-1	Circuit analog of the updated CVSIM model. . . . .	90
C-1	Beat-to-beat averaged patient ABP data (top panel) and Levophed medication (bottom panel). . . . .	96
C-2	Circuit analog of Windkessel model. $P_a$ refers to arterial blood pressure. . . . .	97
C-3	Windkessel estimate of $R_a$ (top panel), beat-to-beat averaged patient ABP data (middle panel), and Levophed medication (bottom panel). . . . .	98
C-4	Windkessel estimate of $R_a$ incorporating the nonlinearity in $C_a$ (top panel), beat-to-beat averaged patient ABP data (middle panel) and Levophed medication (bottom panel). . . . .	99



# List of Tables

2.1	Nominal parameter values for the CVSIM model [4]. . . . .	29
2.2	Comparison between model outputs and reported norms for compartmental pressures, stroke volume and cardiac output [5, 6]. . . . .	35
3.1	Nominal parameter values for the arterial baroreflex model. The values are taken from Davis’s implementation [4]. . . . .	49
4.1	Parameters identified as being well-conditioned by the subset selection algorithm. . . . .	62
4.2	Estimation error statistics for the active parameters under two schemes: estimating only the active parameters with the ill-conditioned ones fixed at their nominal values, and estimating all the model parameters. . . . .	64
4.3	Estimation error statistics for the active parameters with $C_v$ and $C_l^{ed}$ fixed at their actual values. . . . .	66
B.1	Independent Parameters of the CVSIM Model (adapted from Heldt [7]). . . . .	94



# Chapter 1

## Introduction

### 1.1 Motivation

Patient care for the critically ill is provided in dedicated hospital departments known as *Intensive Care Units*, or *ICUs*. Patients suffering from various conditions, such as unstable cardiovascular disease, multiple-organ failure, or severe trauma, are usually admitted to the ICU. Though the reasons behind admissions are varied, ICU patients have one thing in common: they are often in a fragile condition which requires close monitoring of the state of the patient to guide the course of treatment, or to allow for rapid intervention if the patient's state deteriorates.

To help accomplish this, modern ICUs are equipped with a wide range of monitoring equipment, each continuously recording a series of physiological signals. These detailed measurements are supplemented with frequent laboratory tests and imaging studies from different hospital departments. The logistics involved in data collection from different departments and the high volume of data, coupled with poor data integration and organization, complicate and prolong the clinician's task of formulating physiological hypotheses and determining treatment options. However, timely and accurate patient care is of utmost importance in an ICU setting where patients require immediate and often proactive intervention. Thus, the increase in sheer volume of data available and its lack of organization have rendered the

clinical decision-making process inefficient. Presenting all the available information without regard to relevance can often lead to oversight of important factors which can cause serious, possibly fatal, errors in an ICU setting. This phenomenon is generally known as the problem of *information overload* which has contributed to several historical catastrophes including the New York City blackout of 1977 [8].

In addition to the information overload problem, ICUs suffer from inaccurate alarm systems. Bedside alarms sound an alert whenever an individual measured signal exceeds or drops below some predefined values, an event that occurs quite often with no physiological basis, as for example, when excessive patient movement interferes with electrode contacts and position. Individual signals being monitored are usually correlated and interdependent. However, current representation of these signals does not incorporate these relationships, which results in too sensitive an alarm system. In fact, several studies have shown that over 80% of these single-variable alarms are false positives [9], leading to misallocated resources and desensitization to alarms.

The inability of the ICU monitoring systems to evaluate the state of the patient efficiently increases the chances of human error. Donchin et al. [10] conducted a study in which they estimated that 1.7 human errors occur per patient per day in the ICU they observed. One of the reasons for the errors was attributed to difficulties in assessing patient state, a function which is directly affected by the limitations of the current monitoring systems coupled with the information overload problem.

The problems encountered in ICU patient monitoring motivate the use of computational models. Representing a physiological system in a mathematical form aids in understanding how the various components interact with each other to influence the outputs. Computational models tend to synthesize information in one common holistic framework, thereby improving data integration and organization. Given current computational power, computational models can cycle through many iterations of hypothesis-generation and test their compatibility with experimental data in real time. Furthermore, computers tend to be more vigilant than humans. Thus, computational models might be able to learn from clinical data

and help significantly in developing physiological hypotheses regarding a patient's state.

The cardiovascular system has been subjected to various modeling studies (see Section 1.3). There is enough knowledge about the cardiovascular system to formulate mathematical models that describe the major inter-component relationships quite accurately. Such models may be useful in helping to assess patient state, and if so, they can be employed to aid in patient monitoring.

## 1.2 The Cardiovascular System

The human cardiovascular system is responsible for circulating blood throughout the body to perfuse the tissues with nutrients and oxygen, and remove the waste products. The system includes the heart, which acts as a pump, and the blood vessels through which the blood flows (see Figure 1-1).

There are three main kinds of blood vessels: arteries, veins and capillaries. The arteries carry blood from the heart to the tissues at high pressures. As blood is transported to the rest of the body, arteries branch out into smaller vessels through which blood is transported to individual organs. Within the organs, the exchange of oxygen and nutrients takes place through the walls of thin vessels known as capillaries. The veins, which constitute the low-pressure carrying component of the system, transport blood back to the heart.

The heart consists of four chambers - two atria (left and right), each of which is connected to a ventricle. The pumping action of the heart is quasi-periodic in nature, the rhythm of which is governed by electrical impulses generated by the sino-atrial node. A cardiac cycle consists of two regimes of operation: *diastole* and *systole*. During the period of diastole, the ventricles are relaxed and fill with blood, whereas in systole, the ventricles contract and eject blood into the circulation. The left ventricle pumps oxygenated blood to the rest of the body (systemic circulation). After the exchange of nutrients and oxygen, de-oxygenated blood is returned to the right atrium and then the ventricle, which then pumps the blood through the lungs (pulmonary circulation) where gaseous exchange occurs. The newly oxygenated blood is then driven into the left atrium and then ventricle, from where the cycle continues.

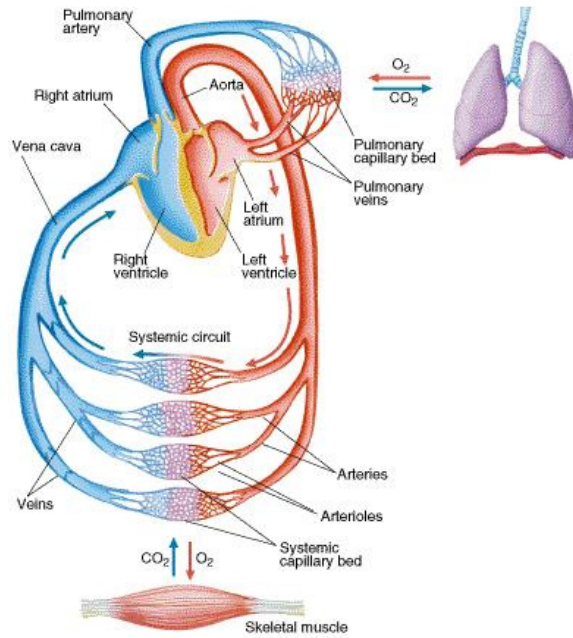


Figure 1-1: The Circulation System [1].

As the cardiovascular system maintains blood flow, a model that accurately represents this system can be used to gain insight into the hemodynamic changes occurring in patients.

### 1.3 Cardiovascular Models and Model-Based Reasoning

An analogy exists between computational models of cardiovascular function and electrical circuits, a parallel that has been exploited since the late 1800's. Moens and Korteweg used transmission-line theory to describe quantitatively the circulation system in 1878. Around twenty years later, Frank introduced the Windkessel model, which consisted of a simple first-order circuit to model arterial dynamics [11]. With the advent and widespread use of digital computing, a wealth of research has been directed towards the development of computational cardiovascular models that adequately represent the underlying physiology and hemodynamics. The models vary in degree of complexity, with the '*Guyton Model*',

consisting of the combined physiological insight of Dr. Guyton and his associates, being the most comprehensive [12].

The purpose behind model development is to gain insight into physiological phenomena within a closed framework. Much of the mentioned modeling work has been directed towards forward-modeling, which consists of constructing computational models capable of producing realistic data. Recently, however, interest has been generated in *inverse-modeling*, or *parameter estimation*, where the model parameters are estimated on the basis of observed data. Various techniques, including gradient-based error minimization using underlying computational models, have been used to estimate cardiac function [13] and arterial parameters [13, 14, 15].

Cardiovascular parameter estimation can provide an integrated framework that can be used to assess the patient's hemodynamic state. Knowledge of the changes in specific parameter values can help monitor patient trajectory and guide clinical interventions. Motivated by the advantages of model-based estimation and reasoning, Zhao developed a set of heuristic algorithms to estimate 7 of the 17 independent parameters in an underlying lumped-parameter, 6-compartment, cardiovascular model [16]. The system evaluated the parameters by iteratively matching the model output to pseudo-patient data. This was achieved by tweaking the model parameters based on some underlying logic using artificial intelligence. The algorithms were tested on steady-state simulated data and were found to perform reasonably. However, such a system cannot be used for continuous monitoring, as the algorithms use certain measurements that are only intermittently available, for example, left ventricular end-diastolic pressure (LVEDP). Moreover, the steady-state assumption is not always valid in unstable patients. In order to help monitor patients continuously, the estimation algorithm has to be devoid of the steady-state assumption and it has to be limited to using what is constantly measurable in an ICU.

## 1.4 Hemodynamic Monitoring in an ICU

Modern day ICUs have the capability to routinely record the following hemodynamic data:

- **Electrocardiograph (ECG):** ECG is a recording of the body surface potentials generated by the electrical activity of the heart. ECG recordings are important indicators of the state of the heart and are extensively used for diagnosis of cardiac conduction abnormalities (arrhythmias), ischemia, infarction, hypertrophy, etc. Moreover, ECG monitors will record heart rate (HR) and rhythm, which are important factors in judging the stability of all patients.
- **Systemic Arterial Blood Pressure (ABP):** ABP is monitored invasively using an arterial line inserted into an accessible artery. The preferred site of insertion is the radial artery on the wrist as it is easily accessible and simple to keep clean. Continuous ABP monitoring is essential as abnormal ABP is indicative of diseased states. In addition, continuous ABP monitoring serves as a feedback to clinical interventions such as medication. The monitoring system records ABP waveforms and also computes derivable quantities such as systolic, diastolic, and mean pressures.
- **Central Venous Pressure (CVP):** CVP waveforms are monitored by inserting a venous catheter into a peripheral vein and by advancing the catheter through the subclavian vein and the superior vena cava. CVP is an important determinant of right ventricular function as it correlates with the filling pressure of the right heart.
- **Pulmonary Artery Pressure (PAP):** The introduction of PAP monitoring has been one of the most popular and important advances in patient monitoring [17]. Although recently PAP recordings have become subjected to increased scrutiny, it is not uncommon to have patients inserted with a Swan-Ganz catheter to record PAP waveforms. The catheter is inserted into a peripheral vein, and it is pushed past the right atrium and ventricle until it enters the pulmonary artery. The tip of the catheter is fitted with a balloon, which, when inflated, obstructs flow and gives a measure of left ventricular filling pressure.
- **Cardiac output (CO)** is an important hemodynamic parameter which can be measured intermittently in an ICU. CO is a measure of the blood volume pumped by the heart

per minute and hence it is an important indicator of cardiac function. CO is usually measured by the thermodilution technique, in which a patient is administered a bolus of cold liquid. The ensuing temperature changes, measured by a thermistor attached to a catheter, are then plotted over time, forming what is known as the thermodilution curve. A measure of CO is obtained by exploiting its inverse relationship to the area under the thermodilution curve.

## 1.5 Thesis Goals and Outline

In this thesis, we explore model-based quantitative methods for estimating selected cardiovascular parameters over time. Tracking the time evolution of these parameters will not only aid in determining patient state, but it may also help in identifying the onset of complications, thereby increasing the quality and effectiveness of patient care. The data used for estimation is limited to what can be monitored continuously in an ICU. This includes waveforms and other derivable quantities of ECG, ABP, CVP, and PAP. The challenge lies in using a small number of observable signals to perform parameter estimation based on an underlying high-detail model. To overcome this difficulty, we focus on estimating only a subset of parameters.

In Chapters 2 and 3, we detail the computational cardiovascular model used for our investigation and we describe its implementation in Simulink.

In Chapter 4, we use synthetic waveform data to estimate cardiovascular parameters using a nonlinear least squares optimization technique along with subset selection - an algorithm that identifies a subset of parameters that can be estimated robustly.

In Chapter 5, we explore a real hemorrhage case. We attempt to track the bleeding rate and the rate of change of peripheral resistance using beat-to-beat averaged data. Accurate knowledge of the values of these two parameters is critical in treating any hemorrhage case.

In Chapter 6, we provide concluding remarks and directions for future research efforts.



## Chapter 2

# The Computational Hemodynamic Model

A strong analogy exists between electric circuits and fluid systems. Computational models of the cardiovascular system are therefore conveniently represented in the form of their circuit analogs. The vessels can be thought of as capacitors with compliances ( $C, \frac{mL}{mmHg}$ ) that store blood volume ( $Q, mL$ ), connected to resistors ( $R, \frac{mmHg \cdot s}{mL}$  or  $PRU$ ) which account for the fluid resistance faced by blood flow. The ventricles can be modeled as capacitors with time varying compliances. During diastole, ventricular compliance is high, which allows the ventricles to store blood volume, thus mimicking the act of being filled. During systole, however, ventricular compliance decreases, thus increasing pressure, which leads to the emptying of the chamber. A periodic compliance function that varies between the diastolic and systolic compliance values can therefore be used to model the pumping action of the heart. Using this circuit analogy, blood volume maps to charge, blood flow rate ( $\dot{q}, mL/s$ ) to current, and pressure ( $P, mmHg$ ) to voltage. In this chapter, we describe the cardiovascular model used and we detail its implementation. The various control loops that regulate the system are described in the next chapter.

## 2.1 Simplifying Assumptions

It would be practically impossible to construct a model with a manageable level of complexity that accounts for all the nuances of cardiovascular function. A great simplifying assumption in this regard is that the cardiovascular system can be represented by a lumped-parameter model. Dispersed networks, such as that of the arteries and arterioles, are thereby modeled using single circuit elements. Lumping the parameters together reduces the ability of the model to represent distributed behavior, such as pulse reflections; however, such detail is currently not the focus of our investigation.

Another simplifying assumption is that most of the circuit elements (apart from the diodes that represent valves) are linear. For the capacitors, this assumption is reasonable over the range of pressures for which the elastic fibers of the vessels are stressed, leading to an approximately linear volume-pressure relationship. Beyond this range, collagen fibers become stressed and add an element of nonlinearity. The systemic arteries, however, exhibit nonlinear compliance over all pressure ranges due to the presence of multiple tensions. Moreover, the pulmonary arterial resistance is notably nonlinear in behavior as well [18]. However, for the sake of simplicity, these elements can be considered as linear without compromising appreciably the ability of the model to represent the cardiovascular system for the purposes of our investigation.

## 2.2 CVSIM

The Cardiovascular Simulator, or *CVSIM*, was originally developed by Davis as an aid in teaching cardiovascular physiology [4]. Figure 2-1 shows the model in its circuit representation. *CVSIM* comprises six compartments which model the left and right ventricles ( $l, r$ ), the systemic arteries and veins ( $a, v$ ), and the pulmonary arteries and veins ( $pa, pv$ ). The atria are excluded from the model because they play no significant hemodynamic role at normal heart rates. During increased heart rates, as may be the case in disease conditions, atrial contraction may contribute significantly to stroke volume. However, the effects of the

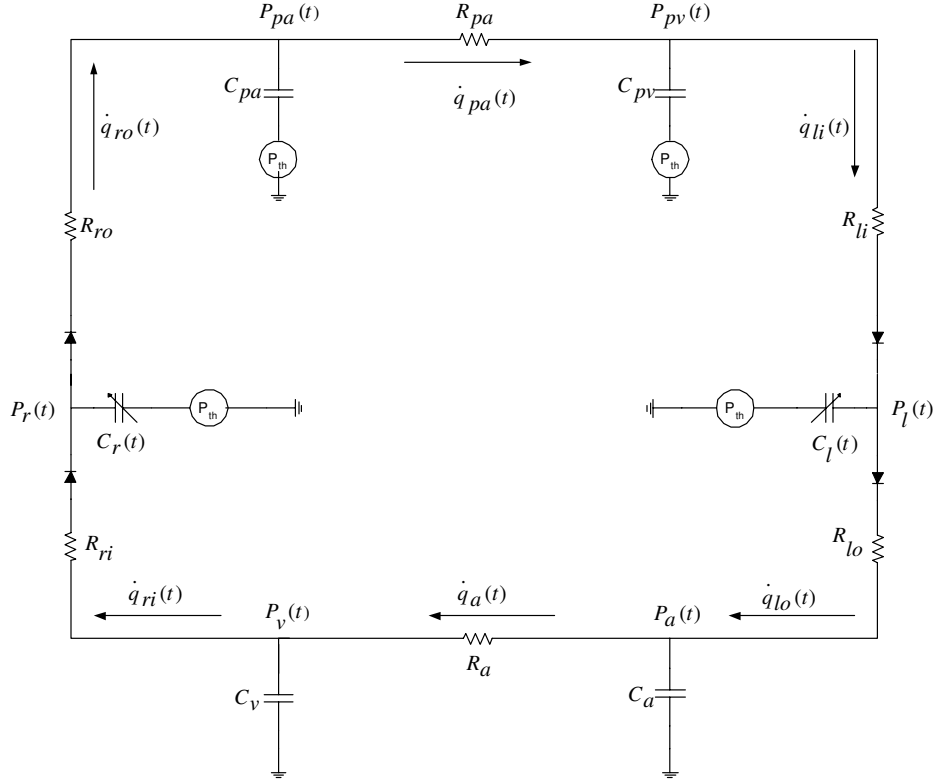


Figure 2-1: Circuit analog of the CVSIM model.

atria can be approximately accounted for by modifying the right ventricular parameters [4].

The ventricles are modeled by time-varying compliances connected to inflow and outflow resistances ( $R_{(l,r)i}$ ,  $R_{(l,r)o}$ ) that represent the resistance encountered by blood flow as it enters and exits the ventricles. The time-varying compliance is completely characterized in our idealized model by the beat period ( $T$ ), and by its minimum (end-systolic ( $es$ )) and maximum (end-diastolic ( $ed$ )) values (see Section 2.3.3). The rest of the compartments are each modeled by a linear capacitor coupled with a linear resistor. The resistances for the systemic and pulmonary veins are lumped with the right and left ventricular inflow resistances respectively. Each capacitor acts as a storage for blood volume, as determined by the characteristic relationship:

$$Q_i = C_i \cdot (P_i - P_i^{ref}) \quad (2.1)$$

where the subscript  $i$  refers to any of the six compartments.  $Q_i$  is referred to as the stressed compartment volume. To represent the volume of the compartment at zero-pressure, each compartment has another volume parameter,  $Q_i^0$ , associated with it. The reference pressure,  $P_i^{ref}$ , is atmospheric for the systemic circulation, and intrathoracic pressure ( $P_{th}$ ) for the rest of the compartments as they reside inside the thorax. Although  $P_{th}$  is known to vary with respiration, it can be modeled reasonably well as a constant equal to its average value. The diodes constitute the only nonlinear elements of the model and act as cardiac valves that ensure uni-directional blood flow through the ventricles.

We chose to use the CVSIM model because of its reasonable level of complexity and its remarkable ability to model normal cardiovascular dynamics. Moreover, it was also previously used successfully to model some steady-state disease conditions, thus demonstrating its ability to model abnormal conditions as well [4, 16].

## 2.3 The Model Implementation

### 2.3.1 The Platform

We developed the model in Simulink<sup>1</sup>, which is a strong tool for simulating dynamic systems. Simulink allows for a good degree of abstraction by providing building blocks with built-in functions and routines. The model becomes easily extendible, which is advantageous for simulating various disease conditions. Another advantage of this platform is the fact that it is automatically interfaced with Matlab, which makes the analysis and presentation of data very convenient.

### 2.3.2 Nominal Parameter Values

The nominal parameter values were determined by Davis for a 70-kg individual [4]. We use his values, which are summarized in Table 2.1.

---

<sup>1</sup>Version 5.0 (R13) dated 20-Jun-2002

Table 2.1: Nominal parameter values for the CVSIM model [4].

Compartment	$C, \frac{mL}{mmHg}$	$Q^o, mL$	$R, \frac{mmHg-s}{mL} (PRU)$
left ventricle ( $l$ )	0.4 – 10	15	0.006 ( $R_{lo}$ - left ventricular outflow resistance)
systemic arteries ( $a$ )	1.6	715	1.0
systemic veins ( $v$ )	100.0	2500	0.01 ( $R_{ri}$ - right ventricular inflow resistance)
right ventricle ( $r$ )	1.2 – 10	15	0.003 ( $R_{ro}$ - right ventricular outflow resistance)
pulmonary arteries ( $pa$ )	4.3	90	0.08
pulmonary veins ( $pv$ )	8.4	490	0.01 ( $R_{li}$ - left ventricular inflow resistance)

**System parameters:**

$$\begin{aligned}
 T &= \frac{5}{6} \text{ s} \\
 P_{th} &= -4 \text{ mmHg} \\
 Q_{total} &= 5000 \text{ mL}
 \end{aligned}$$

### 2.3.3 The Time-Varying Compliance Function

The compliances of the ventricles are based on the ventricular model of Suga and Sagawa [19, 20]. The idealized time evolution of the compliance function is given below, as outlined by Mukkamala [18], in the form of its inverse, called elastance ( $E$ ).

$$E_{l,r}(t) = \begin{cases} \frac{1}{2} \left( \frac{1}{C_{l,r}^{es}} - \frac{1}{C_{l,r}^{ed}} \right) \cdot (1 - \cos(\frac{\pi(t-t_i)}{T_s})) + \frac{1}{C_{l,r}^{ed}} & t_i \leq t < t_i + T_s \\ \frac{1}{2} \left( \frac{1}{C_{l,r}^{es}} - \frac{1}{C_{l,r}^{ed}} \right) \cdot (1 + \cos(\frac{2\pi(t-(t_i+T_s))}{T_s})) + \frac{1}{C_{l,r}^{ed}} & t_i + T_s \leq t < t_i + T_s + T_{ir} \\ \frac{1}{C_{l,r}^{ed}} & t_i + T_s + T_{ir} \leq t < t_{i+1} \end{cases} \quad (2.2)$$

where the subscript  $i$  refers to the  $i^{th}$  cardiac cycle.  $T_s$  and  $T_{ir}$  refer to the systolic time period and the time for isovolumetric relaxation, respectively. These two parameters are related in the following manner:

$$T_s = 0.3\sqrt{T} \quad (2.3)$$

$$T_{ir} = \frac{T_s}{2} = \frac{0.3\sqrt{T}}{2} \quad (2.4)$$

The time period for diastole,  $T_d$ , can therefore be calculated as follows:

$$T_d = T - T_s - T_{ir} = T - 0.45\sqrt{T} \quad (2.5)$$

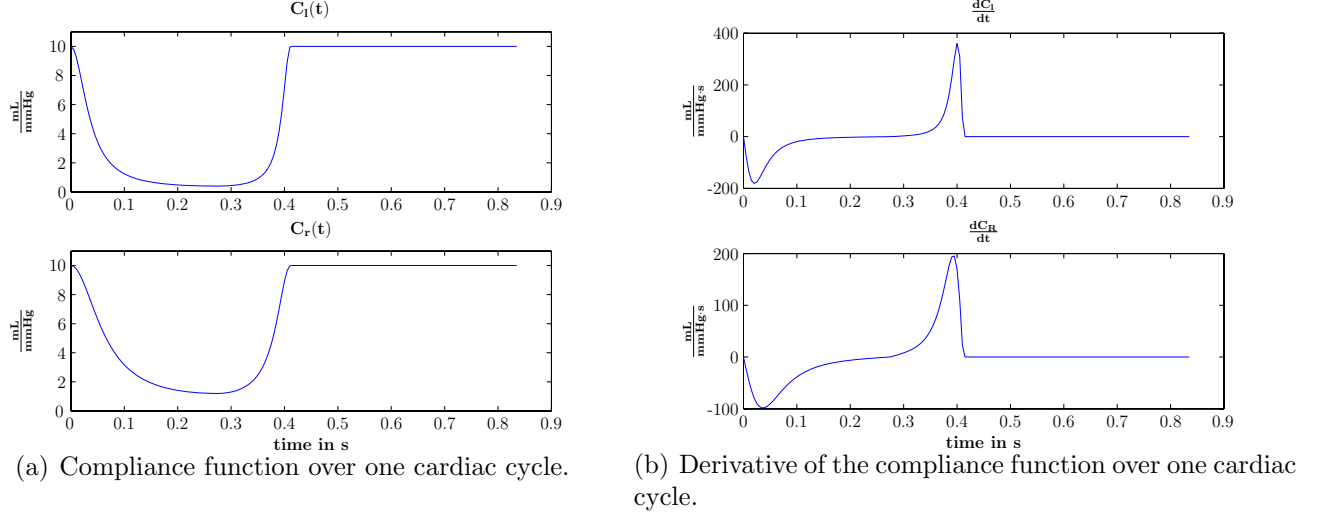


Figure 2-2: Ventricular compliance function and its derivative.

Figure 2-2a shows the compliance function over one cardiac cycle.

### 2.3.4 The Model Dynamics

Applying Kirchhoff's Current Law (KCL) to the circuit topology of the model, the following set of equations is obtained:

$$\frac{dP_l}{dt} = \frac{\dot{q}_{li} - \dot{q}_{lo} - (P_l - P_{th}) \cdot dC_l(t)/dt}{C_l(t)} \quad (2.6)$$

$$\frac{dP_a}{dt} = \frac{\dot{q}_{lo} - \dot{q}_a}{C_a} \quad (2.7)$$

$$\frac{dP_v}{dt} = \frac{\dot{q}_a - \dot{q}_{ri}}{C_v} \quad (2.8)$$

$$\frac{dP_r}{dt} = \frac{\dot{q}_{ri} - \dot{q}_{ro} - (P_r - P_{th}) \cdot dC_r(t)/dt}{C_r(t)} \quad (2.9)$$

$$\frac{dP_{pa}}{dt} = \frac{\dot{q}_{ro} - \dot{q}_{pa}}{C_{pa}} \quad (2.10)$$

$$\frac{dP_{pv}}{dt} = \frac{\dot{q}_{pa} - \dot{q}_{li}}{C_{pv}} \quad (2.11)$$

The compartmental flow rates are obtained from the defining equation for resistors:

$$\dot{q}_{li} = \begin{cases} \frac{P_{pv} - P_l}{R_{li}} & \text{if } P_{pv} > P_l \\ 0 & \text{otherwise} \end{cases} \quad (2.12)$$

$$\dot{q}_{lo} = \begin{cases} \frac{P_l - P_a}{R_{lo}} & \text{if } P_l > P_a \\ 0 & \text{otherwise} \end{cases} \quad (2.13)$$

$$\dot{q}_a = \frac{P_a - P_v}{R_a} \quad (2.14)$$

$$\dot{q}_{ri} = \begin{cases} \frac{P_v - P_r}{R_{ri}} & \text{if } P_v > P_r \\ 0 & \text{otherwise} \end{cases} \quad (2.15)$$

$$\dot{q}_{ro} = \begin{cases} \frac{P_r - P_{pa}}{R_{ro}} & \text{if } P_r > P_{pa} \\ 0 & \text{otherwise} \end{cases} \quad (2.16)$$

$$\dot{q}_{pa} = \frac{P_{pa} - P_{pv}}{R_{pv}} \quad (2.17)$$

Equations 2.6 - 2.11 give the time derivatives of the compartmental pressures, which act as state variables. The system of equations can be solved by discretizing the problem. Given an initial set of pressures, the corresponding flow rates are calculated and used to determine the local gradient information for the pressures. The pressure gradients are then integrated over time to obtain the compartmental pressures at the next time step. Once the new set of pressures is obtained, the cycle continues and the system is evolved iteratively in time. The integration routine used is the standard, fourth-order Runge-Kutta method with a fixed step-size of 0.005s [21]. The fixed step-size is on the order of the smallest time-constant of the system and it is smaller than 0.006s, which was identified as the maximum allowable step-size by Davis [4]. The details of the model implementation outlined here, including the choice of state variables, are similar to previous realizations of CVSIM [4, 18].

### 2.3.5 Initial Conditions

The initial conditions for the state variables are obtained by employing the method used by Davis [4]. A set of linear equations, formulated on the basis of conservation of volume (charge), are solved to obtain the end-diastolic pressures, which are then used as initial conditions for the start of a cardiac cycle:

$$C_l^{ed}(P_l^{ed} - P_{th}) - C_l^{es}(P_l^{es} - P_{th}) = C_r^{ed}(P_r^{ed} - P_{th}) - C_r^{es}(P_r^{es} - P_{th}) \quad (2.18)$$

$$= T_s \frac{P_l^{es} - P_a}{R_{lo}} \quad (2.19)$$

$$= T \frac{P_a - P_v}{R_a} \quad (2.20)$$

$$= T_d \frac{P_v - P_r^{ed}}{R_{ri}} \quad (2.21)$$

$$= T_s \frac{P_r^{es} - P_{pa}}{R_{ro}} \quad (2.22)$$

$$= T \frac{P_{pa} - P_{pv}}{R_{pa}} \quad (2.23)$$

$$= T_d \frac{P_{pv} - P_l^{ed}}{R_{li}} \quad (2.24)$$

$$\begin{aligned} Q_{total} - Q_{total}^o &= C_l^{ed}(P_l^{ed} - P_{th}) + C_a P_a \quad (2.25) \\ &+ C_v P_v + C_r^{ed}(P_r^{ed} - P_{th}) \\ &+ C_{pa}(P_{pa} - P_{th}) + C_{pv}(P_{pv} - P_{th}) \end{aligned}$$

Equations 2.18 - 2.25 are independent and can be solved to obtain the six initial compartmental pressures. Equation 2.18 equates the left and right ventricular stroke volume (volume of blood pumped out by the left and right ventricles during one cycle). Equations 2.19 - 2.24 equate the stroke volume to the average volume of blood that passes through each of the remaining compartments. Equation 2.25 applies the conservation of volume (charge) condition to equate the total distending blood volume to the sum of the stressed volumes of each compartment.

### 2.3.6 Conservation of Volume

The CVSIM model described is a closed system with no external sources or sinks of charge: the amount of charge in the model is completely defined by the initial conditions and must remain constant throughout the simulation. However, when the model was implemented with the state variables as described by Equations 2.6 - 2.11, volume conservation was not observed (see Figure 2-3).

The cause of deviations in volume was traced to numerical errors associated with the time-varying derivative terms  $\frac{dC_l(t)}{dt}$ ,  $\frac{dC_r(t)}{dt}$ , (see Equations 2.6 and 2.9). Figure 2-2b shows a plot of the derivatives of the compliance functions for one cardiac cycle. The derivatives are not well behaved in that they vary dramatically over short periods of time when transitions occur from systole to isovolumetric contraction, and from isovolumetric contraction to diastole. The abrupt changes in the ventricular compliance derivatives lead to numerical integration errors when computing ventricular pressures. Moreover, the magnitudes of the ventricular compliance derivatives are relatively large, which further magnifies the numerical errors. A simple fix to this problem is a change of ventricular state variables to volume, instead of pressure, which removes the dependency on the ventricular compliance derivatives. Equations 2.26 - 2.27 represent the revised state equations for the ventricles:

$$\frac{dQ_l}{dt} = \dot{q}_{li} - \dot{q}_{lo} \quad (2.26)$$

$$\frac{dQ_r}{dt} = \dot{q}_{ri} - \dot{q}_{ro} \quad (2.27)$$

Figure 2-4 shows a time-series plot of the deviation in expected and calculated total blood volume after the change of ventricular state variables. Barring insignificant numerical errors, the change of state variables leads to volume conservation.

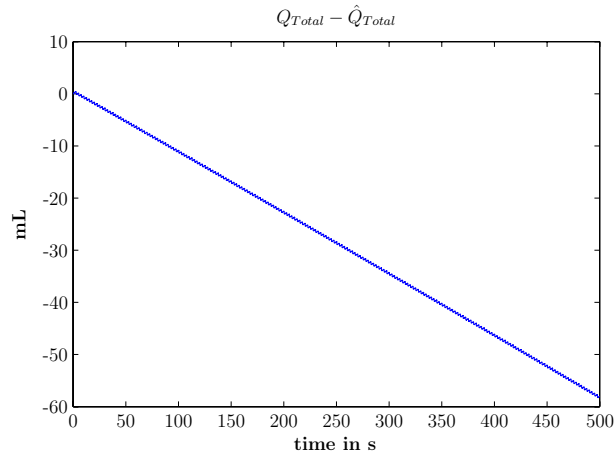


Figure 2-3: Difference between expected total blood volume ( $Q_{Total}$ ) and calculated total blood volume ( $\hat{Q}_{Total}$ ), with left and right ventricular pressure (voltage) as state variables.

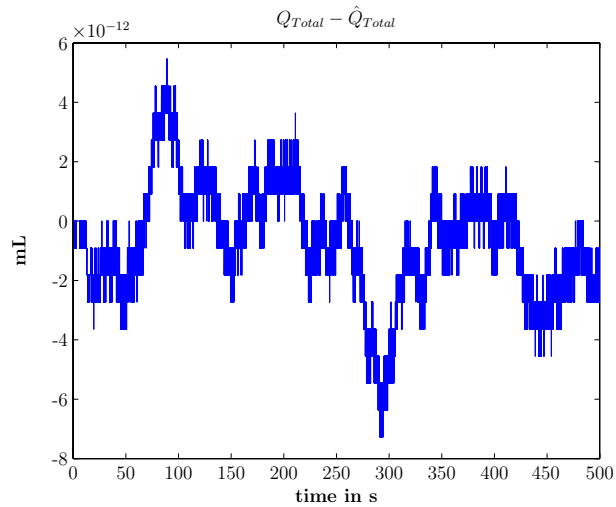


Figure 2-4: Difference between expected total blood volume ( $Q_{Total}$ ) and calculated total blood volume ( $\hat{Q}_{Total}$ ), with left and right ventricular volume (charge) as state variables.

Table 2.2: Comparison between model outputs and reported norms for compartmental pressures, stroke volume and cardiac output [5, 6].

Variable	Reported norm	Simulation
Pressures ( <i>mmHg</i> )		
$P_l$		
Systolic	125	113
Diastolic	8	8
$P_a$		
Systolic	120	112
Diastolic	80	80
$P_v$ (average)	4	7
$P_r$		
Systolic	25	23
Diastolic	4	6
$P_{pa}$		
Systolic	25	22
Diastolic	10	11
$P_{pv}$ (average)	7	9
Volume ( <i>mL</i> )		
Stroke volume	77	74
Cardiac output ( $\frac{L}{min}$ )	5.0	5.3

### 2.3.7 Model Validation

The ability of the CVSIM model to reasonably represent the underlying physiology can be gauged from a comparison of the model outputs, at different time scales, to what is generally observed in humans.

#### Beat-to-Beat comparisons

Table 2.2 shows a comparison of steady-state cardiac output, and beat-to-beat pressure values and stroke volume. The norms listed are for a 70-kg adult as reported by Milnor in Mountcastle's *Physiology* [5, 6].

#### Pulsatile Waveforms

The validation of the intra-beat dynamics is made by plotting the pressure waveforms for all the compartments. Figure 2-5 shows the plots for all the compartmental pressures for a

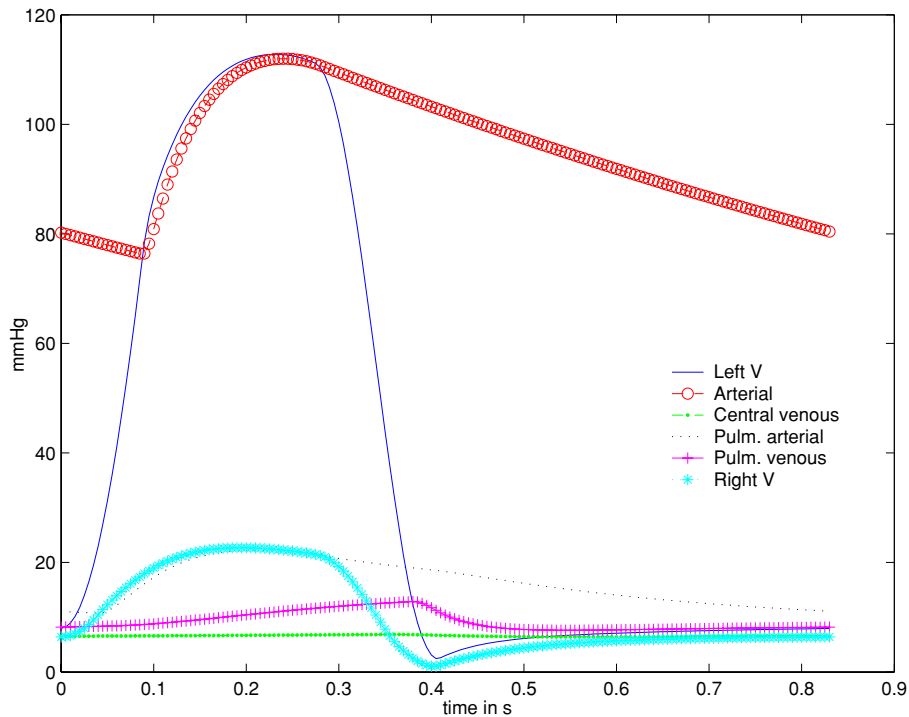


Figure 2-5: Pulsatile pressure waveforms for a single beat.

single beat. On the whole, the pressure waveforms look similar to the actual data obtained by catheterization. The pressure magnitudes and time-constants involved seem reasonable, thus validating the choice of parameter values used. However, expected differences, such as the absence of reflected waves due to the neglect of distributed (traveling wave) effects, caused by the lumping of parameters, are visible.

### 2.3.8 Interstitial Fluid Compartment

Body fluid is divided into two distinct categories: intracellular and extracellular fluid. As the name suggests, intracellular fluid consists of the volume within the cells, which forms approximately  $\frac{2}{3}$  of the total body fluid. Extracellular fluid is further divided into *interstitial fluid* and blood *plasma*. The division is such that in steady state, around  $\frac{11}{14}$  of the extracellular volume resides in the interstitial space, whereas the rest is blood plasma [2]. Figure

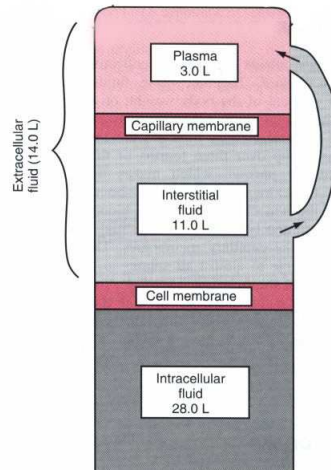


Figure 2-6: Volume distribution for an average 70-*kg* adult. Approximately 60% of body mass is fluid. This percentage can vary depending on age, sex, and obesity [2].

2-6 shows the distribution of fluid volume for an average 70-*kg* adult.

The fluid in plasma constantly interacts with the interstitial space through the capillary pores; however, the CVSIM model does not represent this communication. In steady-state, the absence of the interstitial compartment does not significantly inhibit the ability of the model to represent the underlying physiology, as no net exchange of volume takes place between the two compartments. However, during disease conditions, such as hemorrhage, or during clinical interventions, such as administration of fluid boluses, the role of the interstitial compartment becomes significant. In this section, we describe the addition of the interstitial fluid compartment (*int*), and we detail the derivation of the nominal parameter values associated with the compartment<sup>2</sup>.

---

<sup>2</sup>Note: The interstitial compartment is used only in Chapter 5, when matching simulated data to actual patient data.

## Model Addition

The interstitial fluid compartment is represented by an additional resistor and capacitor ( $R_{int}, C_{int}$ ), connected between the systemic arteries and veins (see Figure 2-7). The capacitor models the volume storage ability of the interstitial fluid space, whereas the resistor models the resistance faced by the fluid when diffusing between the two compartments.

The nominal value for  $C_{int}$  can be determined using the following logic, which analyzes the fluid dynamics before and after the administration of a fluid bolus<sup>3</sup> (saline, for example):

- In steady-state,  $P_v = P_{int}$ , as no net exchange of volume takes place. Consider an initial (*i*) steady-state where  $P_{int}^i = P_v^i = P$ .
- After intra-venous administration of a fluid bolus  $\Delta V$ , a new steady-state will be reached where  $\frac{11}{14}$  of the bolus volume will diffuse into the interstitial space, whereas  $\frac{3}{14}$  will remain in the circulatory system. The veins form the largest blood reservoirs of the circulatory system, storing 64% of the volume [2], so 64% of the fraction of the bolus volume remaining in the intra-vascular space will reside in the veins once the new steady-state has been reached. Since compartmental pressure can be expressed as a ratio of volume to compliance (see Equation 2.1), the following set of equations is obtained when equating the final (*f*) steady-state pressures  $P_{int}^f$  and  $P_v^f$ :

$$P_{int}^f = P_v^f$$

$$P + \frac{11}{14} \cdot \Delta V \cdot \frac{1}{C_{int}} = P + \frac{3}{14} \cdot \Delta V \cdot 64\% \cdot \frac{1}{C_v}$$

$$C_{int} = \frac{11}{14} \cdot \frac{14}{3} \cdot \frac{100}{64} \cdot C_v$$

Using the nominal value  $C_v = 100 \frac{mL}{mmHg}$ ,  $C_{int} \approx 573 \frac{mL}{mmHg}$ .

We use the the same analysis, which considers the dynamics after the administration of a fluid bolus, to determine the value of  $R_{int}$ . The nominal  $R_{int}$  value can be resolved using

---

<sup>3</sup>We assume the administration of isotonic fluids which redistribute between the intravascular and interstitial spaces only [22].

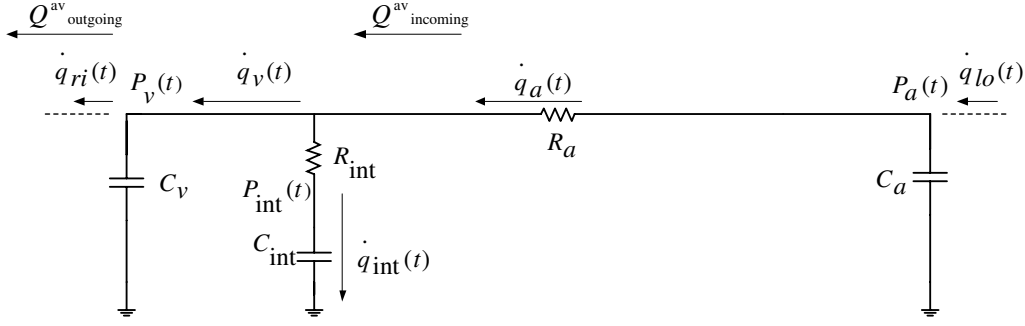


Figure 2-7: Addition of the interstitial compartment between the systemic arteries and veins.

the time-constant involved in the transfer of fluid volume between the interstitial space and the circulatory system. Based on an extensive literature review, Heldt determined that the time-constant for diffusion to and from the interstitial space is the same, with a nominal value  $\tau_{int} = (4.6 \pm 0.4) \text{ min}$  [7].

In the circuit representation of the model, the topology is such that the venous charge decay (post-administration of a fluid bolus) does not follow a simple RC time-constant. Therefore, it is not trivial to determine an analytical formula for the effective time-constant which can be used to pinpoint the best  $R_{int}$  value. To overcome this problem, we assume that on a beat-to-beat averaged basis during the transient, the charge flowing in from the arterial side ( $Q_{incoming}^{av}$ ) is offset by the charge flowing into the right ventricle ( $Q_{outgoing}^{av}$ , see Figure 2-7). With this assumption, the added venous charge redistributes itself between  $C_v$  and  $C_{int}$ , which are connected in series through  $R_{int}$ . This configuration leads to the following approximate value for  $R_{int}$ :

$$\tau_{int} = 276s$$

$$R_{int} \cdot \frac{C_v C_{int}}{C_v + C_{int}} = 276s$$

$$R_{int} \approx 3.2PRU$$

Next, we carried out several simulations of fluid bolus administration in which  $R_{int}$  was

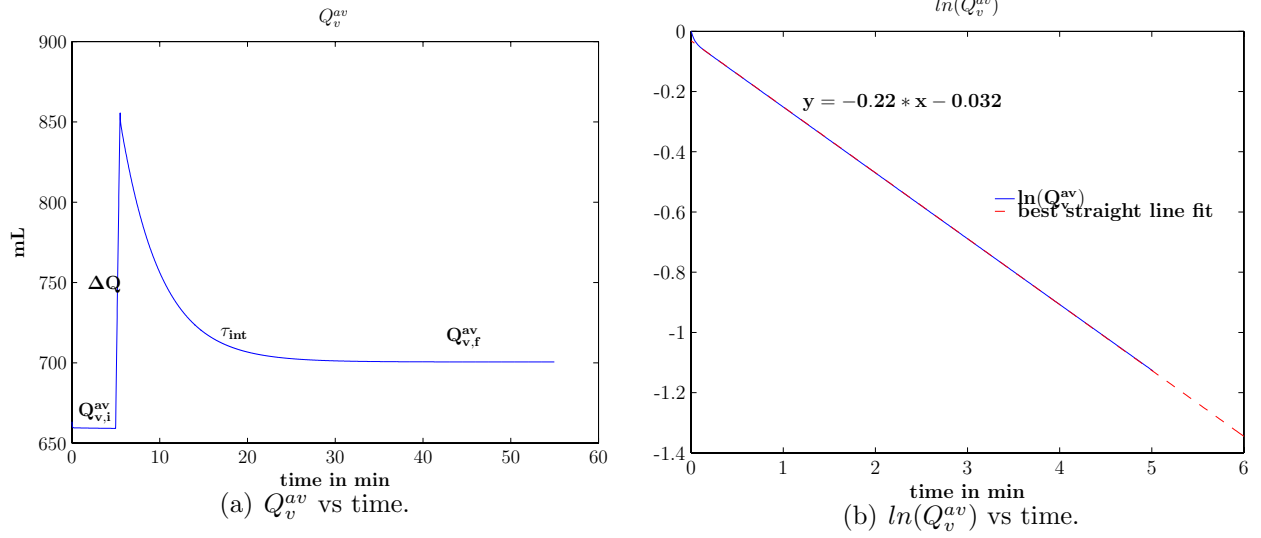


Figure 2-8: Beat-to-beat averaged venous charge ( $Q_v^{av}$ ) vs time. Sub-figure (a) shows the plot of  $Q_v^{av}$  vs time before and after the administration of a fluid bolus. Sub-figure (b) shows the plot of  $\ln(Q_v^{av})$  vs time, and its best straight line fit, after the administration of a fluid bolus. The time-constant for the charge decay is the reciprocal of the slope of the best straight line fit:  $\tau_{int} \approx 4.5$  min.

varied around its approximate value of 3.2 PRU. Based on simulation results,  $R_{int} = 2.3$  PRU yielded a venous charge decay time-constant of approximately 4.5 mins. Hence, a nominal value of 2.3 PRU was assigned to  $R_{int}$ . Figure 2-8 shows the plot of simulated venous volume *vs* time, which captures the dynamics induced by a fluid bolus administration. Figure 2-9 shows a plot of the difference between  $Q_{incoming}^{av}$  and  $Q_{outgoing}^{av}$ . We observe that this difference is indeed small compared to the venous charge decay. Thus, the assumption we made in approximating a value for  $R_{int}$  is verified to be reasonable.

The addition of the interstitial fluid compartment adds another state variable to the model. See Appendix A for the details of the new model equations.

### 2.3.9 Concluding Remarks

Though the CVSIM model does not capture the fine details of cardiovascular function, it is a reasonable model to start investigating the use of parameter estimation as an aid in

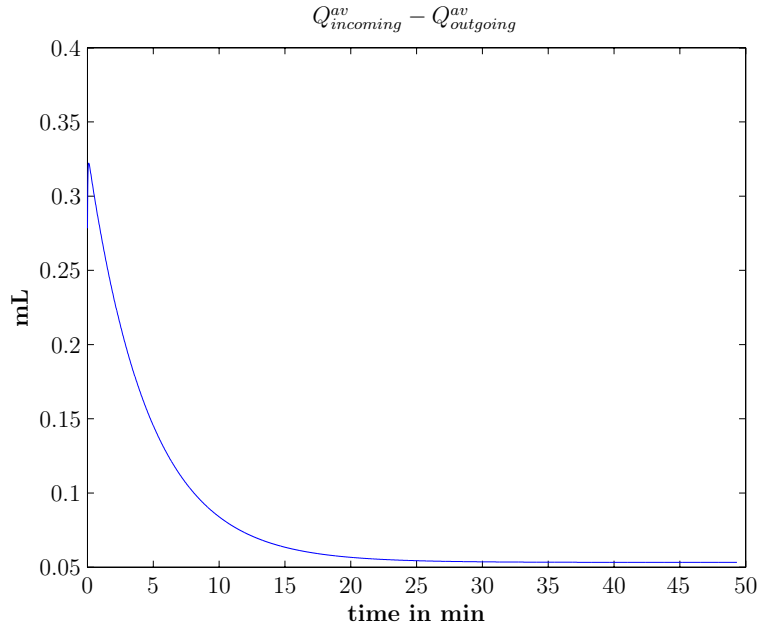


Figure 2-9:  $Q_{incoming}^{av} - Q_{outgoing}^{av}$  after the administration of a fluid bolus.

patient monitoring. Since the overall behavior of the model is similar to the underlying physiology, there is credibility in the use of the system. However, various additions to the model have been proposed, including the use of inductors to model the inertial effects of blood [13]. Moreover, the systemic circulation has also been modeled as a distributed set of parallel compartments, as opposed to a single compartment, in order to include the individual effects of prominent arteries and veins [7]. Nevertheless, there is a clear trade-off between model complexity and ability to represent minute details. The CVSIM model strikes a balance by providing a system that is of manageable complexity, and reasonable in its ability to represent the cardiovascular system.



# Chapter 3

## The Cardiovascular Control System

The cardiovascular system forms the lifeline for cell survival as it transports oxygen and nutrients. The system maintains its critical homeostasis by adapting dynamically to meet the current needs of the body and to counteract hemodynamic perturbations. For example, in the absence of a control system, the commonplace act of regaining the head-up posture from a supine state causes the blood pressure at the level of the heart to drop to such a degree that one might faint. In the presence of cardiovascular control, however, changes in posture are activities that we perform seemingly effortlessly without even noticing the stress that we impose upon the cardiovascular system.

In order to accomplish its task, the cardiovascular system exerts control at both local and global levels. Local control includes the modulation of vascular resistance by tissue beds to maintain adequate blood flow in a specific region. Global control, on the other hand, involves the regulation of hemodynamic variables to maintain overall pressure. The reflex mechanisms involved in control span many time scales, from the fast neurally-mediated (seconds to minutes) actions to the slower hormonally-mediated effects (hours and even days) [2].

In order to faithfully track patient state continuously, we are interested in modeling the short-term cardiovascular control to clinical interventions and to changes in the degree of a disease condition. In this chapter, we describe the arterial baroreflex, which is a principal

component of short-term neurally-mediated control, and we outline its implementation in our simulator<sup>1</sup>. Furthermore, we qualitatively validate the baroreflex function by simulating certain disease conditions.

## 3.1 Arterial Baroreflex

Our representation of the arterial baroreflex is based on Davis’s extension of deBoer’s work [4, 23], with certain changes in implementation that are described in the next section.

The arterial baroreflex is a negative feedback system that aims to maintain ABP around a particular set-point. The afferent leg of the system includes pressure sensors, known as baroreceptors, located in the aortic arch and the carotid sinuses. These receptors sense ABP and transmit this information via afferent fibers to the brain, where the deviation in ABP from the set-point is mapped to sympathetic ( $\alpha$  and  $\beta$ ) and parasympathetic activity. Increased  $\alpha$ -sympathetic action leads to increased peripheral resistance and decreased zero-pressure venous volume, while increased  $\beta$ -sympathetic action causes an increase in cardiac contractility and heart rate. Parasympathetic action affects the heart rate in a manner opposite to  $\beta$ -sympathetic action; an increase in parasympathetic activity reduces the heart rate instead of increasing it. Figure 3-1 presents a block diagram of the arterial baroreflex system.

## 3.2 Implementation

Previous implementations of the baroreflex mechanism adopted relatively coarse time-steps for the control system as compared to the rest of the cardiovascular model [4, 18]. It was deemed computationally inefficient for the reflex system to react to every sample of ABP, as pulsatile ABP is bandlimited to frequencies below ten times the mean heart rate, while the frequency response of the cardiovascular regulatory mechanism is bandlimited to frequencies

---

<sup>1</sup>Several other short-term control mechanisms exist, including the cardiopulmonary reflex. However, as we are primarily interested in responses to hypotensive stimuli (see Section 4.1.5), the arterial baroreflex response is likely to dominate.

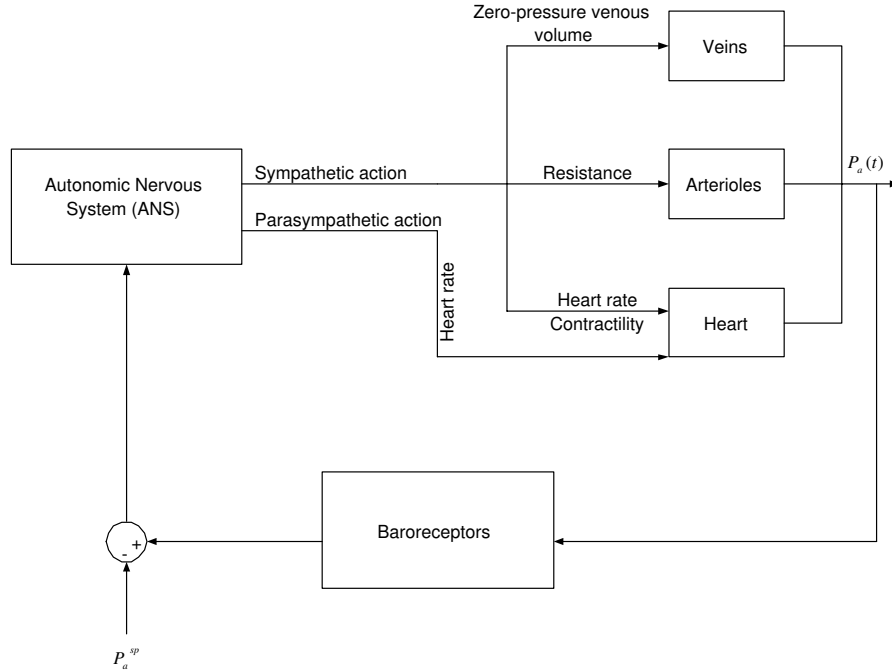


Figure 3-1: Block diagram of the arterial baroreflex system.  $P_a^{sp}$  is the set-point pressure that the system is aiming to maintain.

less than the mean heart rate [18]. Thus, in Davis’s model of the baroreflex, pulsatile ABP was averaged over 0.5 s and then sampled at 0.5 s [4]. This implementation, however, leads to aliasing, as the frequency content above 1 Hz is not sufficiently filtered by the 0.5 s running average filter. A subsequent implementation by Mukammala [18] averaged the pulsatile ABP over 0.25 s and then sampled it at 0.0625 s, thus reducing the aliasing effects. In order to more completely remove the effects of aliasing, we decided to implement the control system in continuous-time.

### 3.2.1 Preprocessing and Error Calculation

Since the cardiovascular regulatory mechanism responds to low-frequency fluctuations of ABP from a set-point, the pulsatile ABP signal is first low-pass filtered to remove the strong frequency content at, and above, the mean heart rate<sup>2</sup>. Next, the low-pass filtered ABP signal

<sup>2</sup>In principle, the low-pass filter should not be required as the physiological control system response itself is bandlimited to frequencies below the mean heart rate. However, as shown in Section 3.2.2, the response

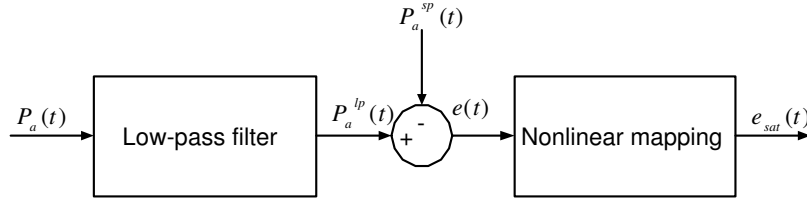


Figure 3-2: Block diagram depicting the preprocessing involved.

$P_a^{lp}(t)$  is subtracted from the set-point to produce the error signal  $e(t)$ , which then is passed on to a nonlinear mapping block that represents the baroreflex saturation characteristic [24]. As the autonomic nervous system exhibits a limiting behavior in its action, the following mapping is applied to  $e(t)$  [23]:

$$e_{sat}(t) = 18 \arctan\left(\frac{e(t)}{18}\right) \quad (3.1)$$

This mapping restricts the input to the effector mechanism to approximately  $\pm 28$  mmHg. Figure 3-2 illustrates the preprocessing mechanism.

### 3.2.2 Effector Mechanism

#### Control Filters

The effector mechanisms are modeled as a linear combination of two LTI filters which represent the sympathetic ( $\alpha$  and  $\beta$ ) and the parasympathetic limbs of the autonomic nervous system. The filters are defined by their unit-area impulse responses,  $s(t)$  (sympathetic) and  $p(t)$  (parasympathetic). Figure 3-3 illustrates  $s(t)$  and  $p(t)$  along with their Fourier transforms.

The filters were implemented using Simulink's continuous-time blockset, which allows for the representation of rational transfer functions and continuous-time delays. The transfer

---

of the estimated control system does not sufficiently attenuate the strong, high-frequency content present in the ABP waveform.

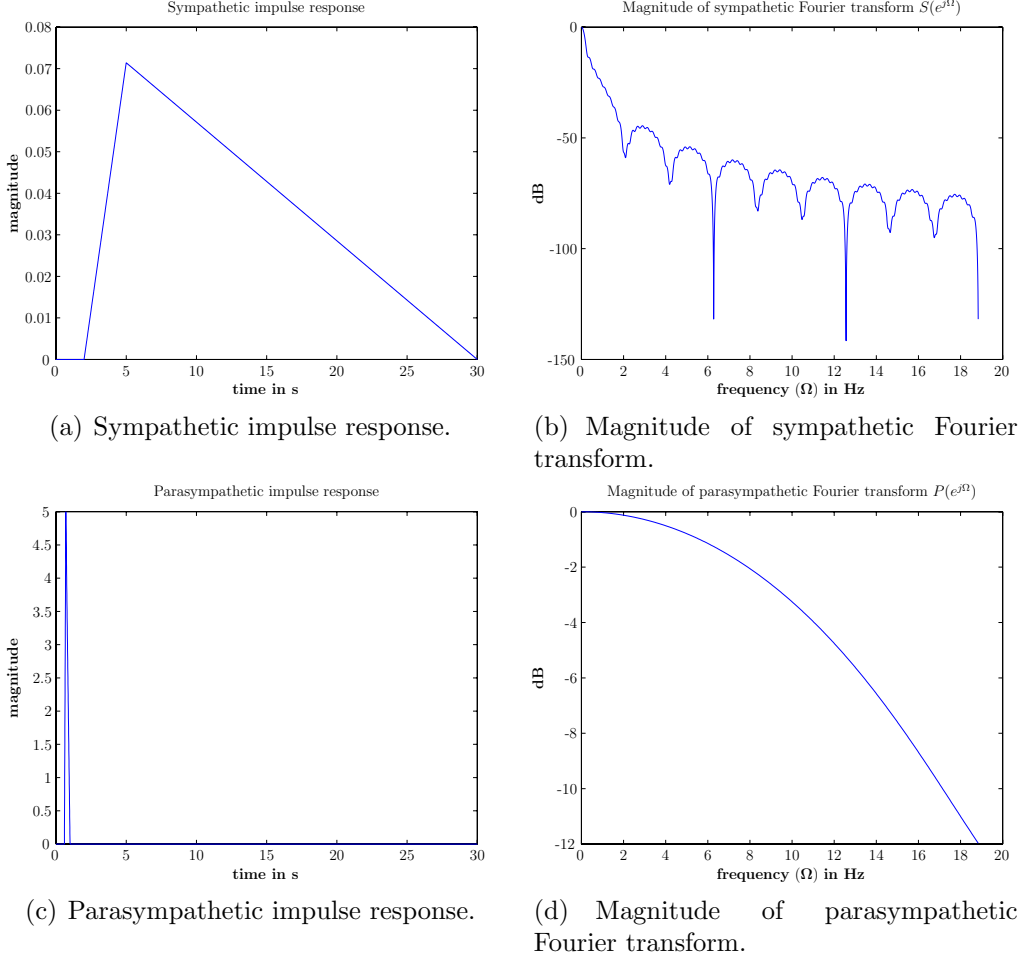


Figure 3-3: Impulse response and magnitude of Fourier transform of sympathetic and parasympathetic filters. The impulse responses are estimated from canine data [3].

functions for the control filters are given as follows:

$$S(s) = \frac{1}{350s^2}e^{-30s} - \frac{2}{75s^2}e^{-5s} + \frac{1}{42s^2}e^{-2s} \quad (3.2)$$

$$P(s) = \frac{-200}{3s^2}e^{-\frac{7s}{10}} + \frac{50}{s^2}e^{-\frac{6s}{10}} + \frac{50}{3s^2}e^{-s} \quad (3.3)$$

## Autonomic Mediation

Autonomic mediation is executed by convolving  $e_{sat}(t)$  with a linear combination of  $s(t)$  and  $p(t)$  to obtain  $\Delta X(t)$ , which is the control system contribution to each effector variable  $X(t)$

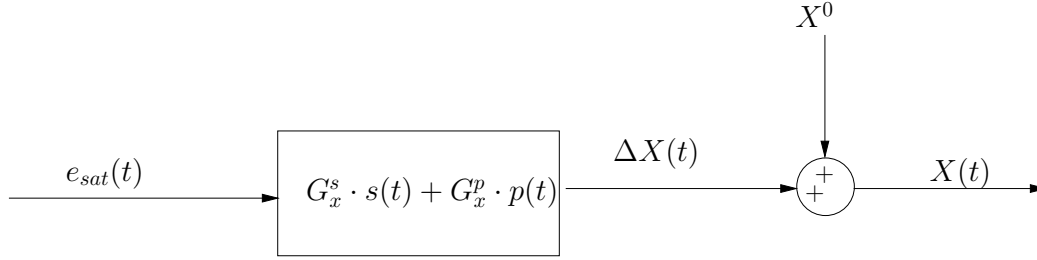


Figure 3-4: Diagrammatic representation of the effector mechanism depicting autonomic mediation.

(see Figure 3-4).  $G_X^s$  and  $G_X^p$  represent the scalings of the unit area impulse responses  $s(t)$  and  $p(t)$  respectively, where  $X$  denotes the effector variable (see Table 3.1 for a summary of the control system parameters). The output of the control filters is then added to the nominal value of the effector variable,  $X^0$ , in order to yield the value of the variable at the current time-step.

The effector limbs corresponding to heart rate, zero-pressure venous volume, and peripheral resistance are all updated every simulation time step. Ventricular contractility, on the other hand, is updated every beat, since the contractility variables are used to define the compliance function (see Section 2.3.3), and hence must remain constant for the entire beat. The onset time for the start of a cardiac-cycle, which begins with ventricular contraction, is determined through an Integral Pulse Frequency Modulation (IPFM) model. The IPFM model integrates heart rate over time until the integral reaches a threshold, after which ventricular contraction starts. The integral is then reset to zero and the process repeats itself (see Heldt [7] for a more detailed description of the IPFM model).

## Stability Issues

When the control system was implemented using Simulink's continuous-time blockset, the parasympathetic implementation turned out to be unstable. Figure 3-5 shows the open-loop step responses of the implemented filters.

In order to obtain a stable implementation of the parasympathetic filter, Padé approximations were used to convert continuous-time delays to rational transfer functions. The

Table 3.1: Nominal parameter values for the arterial baroreflex model. The values are taken from Davis's implementation [4].

<b>Reflex limb</b>		$G^s$	$G^p$
RR-interval	$\frac{ms}{mmHg}$	9	9
Left ventricular contractility	$\frac{mL}{mmHg^2}$	0.007	0
Right ventricular contractility	$\frac{mL}{mmHg^2}$	0.021	0
Peripheral resistance	$\frac{PRU}{mmHg}$	-0.011	0
Zero-pressure venous volume	$\frac{mL}{mmHg}$	26.5	0

---

$P_a^{sp} = 94 \text{ mmHg}$

---

first-order Padé approximation is given as follows:

$$e^{sx} \approx \frac{1 - sx/2}{1 + sx/2} \quad (3.4)$$

Using this approximation, the parasympathetic transfer function can be approximated as follows:

$$\begin{aligned}
 P(s) &= \frac{-200}{3s^2} e^{\frac{-7s}{10}} + \frac{50}{s^2} e^{\frac{-6s}{10}} + \frac{50}{3s^2} e^{-s} \\
 &\approx \frac{-200}{3s^2} \cdot \frac{1 + 7s/20}{1 - 7s/20} + \frac{50}{s^2} \cdot \frac{1 + 6s/20}{1 - 6s/20} + \frac{50}{3s^2} \cdot \frac{1 + s/2}{1 - s/2} \\
 &\approx \frac{1}{0.0525s^3 + 0.43s^2 + 1.15s + 1}
 \end{aligned} \quad (3.5)$$

Figure 3-6a shows the desired parasympathetic impulse response overlaid on the one obtained with the first-order Padé approximation. We observe that while the approximation captures the peak action time, it fails to accurately model the magnitude, initial delay, and the end-response time. In order to correct some of these inadequacies, the response was localized in time by expanding in frequency to obtain what is labeled as the 'tweaked' response. However, only minor improvements were observed. Clearly, the first-order Padé

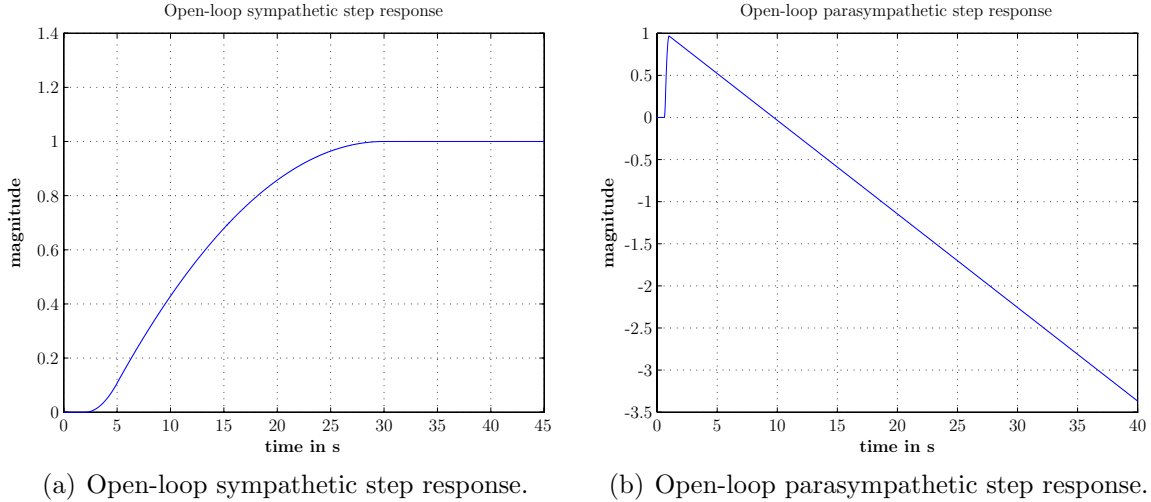
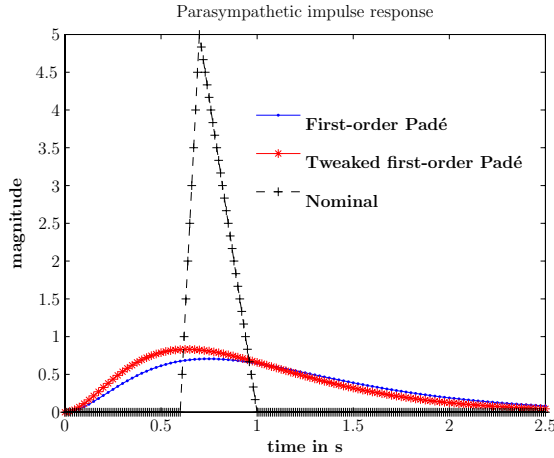


Figure 3-5: Open-loop step responses of sympathetic and parasympathetic filters as implemented using Simulink.

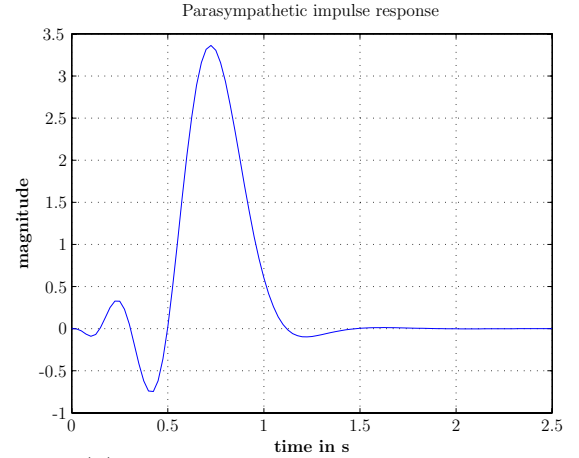
approximation is not sufficient. Therefore, higher-order approximations were used to model better the parasympathetic response. Figure 3-6b shows the impulse response obtained with the fifth-order Padé approximation. This higher-order approximation maintains the integrity of the magnitude and response times, and thus is better able to model the desired response. Figure 3-7 shows a comparison of the open-loop step response of the desired parasympathetic filter, and its first- and fifth-order Padé approximations. The fifth-order Padé approximation is seen to be a viable one as it closely follows the desired response.

### Parasympathetic Response Simplification

Since the parasympathetic impulse response lasts for only a fraction of a heart beat, we tried replacing it with two simplifying approximations: a simple gain, and a pure delay followed by a gain. The closed-loop performances using the simplifications and the fifth-order Padé approximation were compared for two simulated disease conditions: hemorrhage, and left MI (see Section 3.3). Figure 3-8 shows the closed-loop output of the parasympathetic block when using different approximations for the filter. We observe that there is no visible difference amongst the block outputs, indicating that the parasympathetic filter can be represented by



(a) Nominal response and its first-order Padé approximations.



(b) Fifth-order Padé approximation.

Figure 3-6: Nominal parasympathetic impulse response and its Padé approximations.

a simple gain for closed-loop studies.

### 3.3 Qualitative Validation

The control system was validated qualitatively by observing its response to certain disease conditions.

#### 3.3.1 Hemorrhage

A case of hemorrhage was simulated for 30 mins with a blood loss rate of  $1 \frac{L}{Hr}$ . The blood leakage was created by adding a branch to the arterial side of the model, which provided a path for blood to exit the system at a constant rate. Figure 3-9 illustrates how the various pressures change versus time and how the control system responds. The bleeding causes the pressures to fall, thereby activating the control system, which increases the heart rate, peripheral resistance and ventricular contractility, and decreases zero-pressure venous volume. All the mentioned actions executed by the control system serve to increase ABP, hence the control system responds as expected.

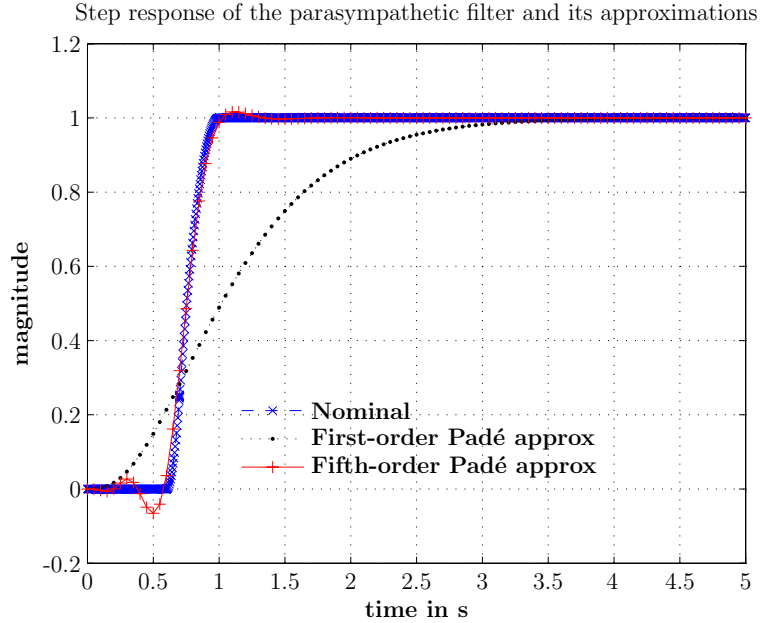


Figure 3-7: Open-loop step response comparison of the nominal parasympathetic filter and its approximations.

### 3.3.2 Left Myocardial Infarction (MI)

A left myocardial infarction was simulated by disconnecting the left end-systolic compliance ( $C_l^{es}$ ) from the control system. This compliance was then explicitly changed from its nominal value of 0.4 to  $1.8 \frac{mL}{mmHg}$  according to a ramp function over the period of a minute. Figure 3-10 shows the plots of the various pressures along with the control system response. Increasing  $C_l^{es}$  decreases the contractility of the left ventricle which causes ABP to drop. Consequently, the control system increases heart rate, peripheral resistance and right ventricular contractility, and decreases the zero-pressure venous volume. Once  $C_l^{es}$  reaches the value of  $1.8 \frac{mL}{mmHg}$  and remains constant, the control system output levels off, indicating how the short-term control system eventually adapts to a disease condition.

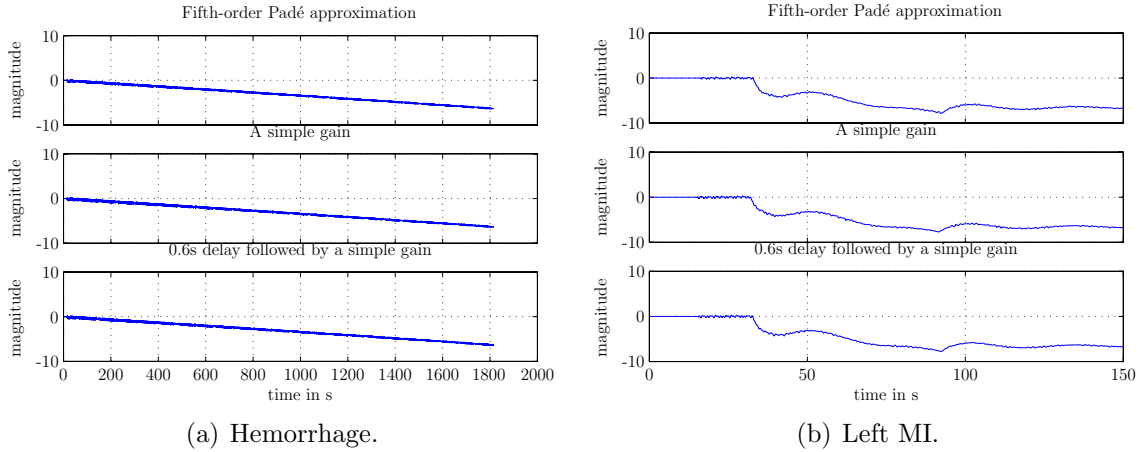
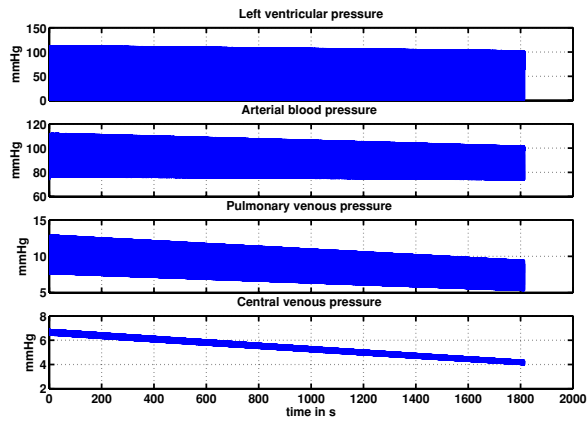


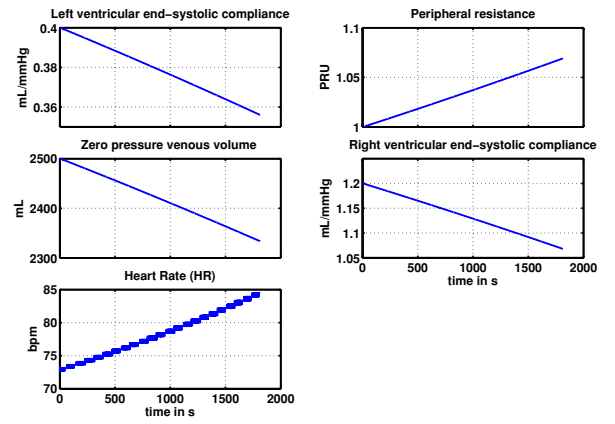
Figure 3-8: Parasympathetic block output during hemorrhage and left MI simulations using different approximations for the parasympathetic filter.

### 3.4 Concluding Remarks

The arterial baroreflex adds an element of reality to the model by implementing short-term cardiovascular control. This addition enhances the model’s ability to represent sudden physiological changes more accurately. With the implementation and qualitative validation of the control system, the model construction is complete, and we can now turn our focus to parameter estimation.

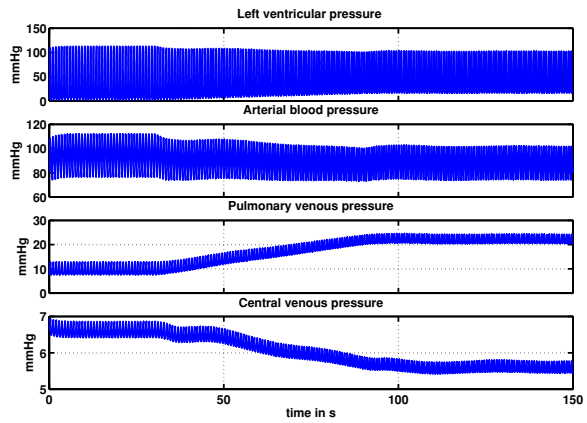


(a) Pressure waveforms versus time.

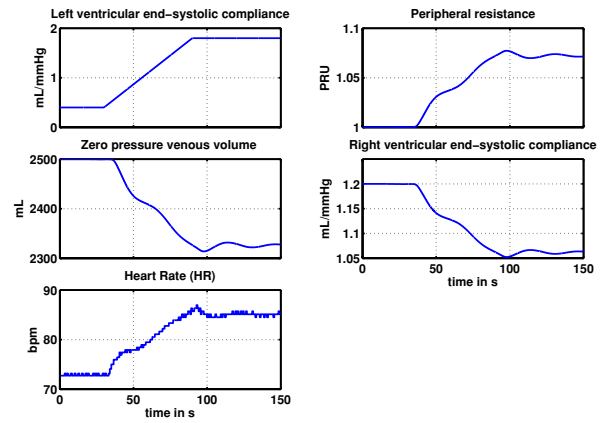


(b) Effector variables versus time.

Figure 3-9: Hemorrhage simulation.



(a) Pressure waveforms versus time.



(b) Effector variables versus time.

Figure 3-10: Left MI simulation.

# Chapter 4

## Parameter Estimation using Waveform Data

The previous chapters were focused on the topic of forward-modeling: we outlined and described the implementation of a pulsatile cardiovascular model that is capable of simulating both normal and abnormal physiology. In this chapter, we tackle the problem of *inverse-modeling* or parameter estimation using waveform data.

Given observable patient data in the form of ABP, CVP, and PAP signals, we would like to estimate the underlying parameters of the model in an effort to track patient state. The observable signals, however, are generally not rich enough to allow for the estimation of all the parameters. This leads to an *ill-conditioned* estimation problem. To overcome the ill-conditioning, we employ subset selection, a methodology that improves the conditioning of the problem by reducing the dimensionality of the estimation problem. Such a scheme was successfully adopted by Heldt [7] to estimate cardiovascular parameters during transient responses to head-up tilt, using a more complex underlying computational model.

First, we give a general outline of a nonlinear least squares optimization technique. Next, we illustrate the problem of ill-conditioning, and subsequently we describe the subset selection solution to improve the conditioning of the problem. Finally, we describe the set-up of the estimation experiments we performed using both steady-state and transient data, and

we present their results.

## 4.1 Nonlinear Least Squares and Subset Selection

### 4.1.1 Nonlinear Least Squares Optimization

In the context of parameter estimation, the nonlinear least squares optimization method iteratively arrives at the best estimates for the parameters of an underlying system by minimizing the error between the model output and the observation. Let  $\mathbf{r}(\boldsymbol{\theta}) = \hat{\mathbf{y}}(\boldsymbol{\theta}) - \mathbf{y}$  denote the residual error, where  $\hat{\mathbf{y}}(\boldsymbol{\theta}) \in \mathbb{R}^n$  corresponds to the model output, which is a function of the parameter vector  $\boldsymbol{\theta} \in \mathbb{R}^m$ , and where  $\mathbf{y} \in \mathbb{R}^n$  refers to the observation (or data) vector. The cost function we try to minimize is a weighted sum of squares of residual errors and is given as follows:

$$\Phi(\boldsymbol{\theta}) = \frac{1}{2}(\mathbf{r}^T \mathbf{Q} \mathbf{r}) \quad (4.1)$$

where  $\mathbf{Q} \in \mathbb{R}^{n \times n}$  is a positive definite matrix of weights, usually diagonal, that weighs the individual error components<sup>1</sup>.

The second-order Taylor series expansion  $\Psi(\boldsymbol{\theta})$  of  $\Phi(\boldsymbol{\theta})$  gives a good approximation of the cost function for small perturbations of  $\Delta\boldsymbol{\theta} = \boldsymbol{\theta}_1 - \boldsymbol{\theta}_0$  around the initial estimate  $\boldsymbol{\theta}_0$ .  $\Psi(\boldsymbol{\theta})$  is given as follows:

$$\Psi(\boldsymbol{\theta}) = \Phi(\boldsymbol{\theta}_0) + \left[ \frac{\partial \Phi}{\partial \boldsymbol{\theta}} \right]_{\boldsymbol{\theta}_0} \Delta\boldsymbol{\theta} + \frac{1}{2} \Delta\boldsymbol{\theta}^T \left[ \frac{\partial^2 \Phi}{\partial \boldsymbol{\theta}^2} \right]_{\boldsymbol{\theta}_0} \Delta\boldsymbol{\theta} \quad (4.2)$$

where  $[\partial\Phi/\partial\boldsymbol{\theta}]_{\boldsymbol{\theta}_0}$  and  $[\partial^2\Phi/\partial\boldsymbol{\theta}^2]_{\boldsymbol{\theta}_0}$  denote the matrices of first- and second-order derivatives evaluated at the current best estimate  $\boldsymbol{\theta}_0$ ; these matrices are respectively termed the *Jacobian* (or *gradient*) and *Hessian* matrices. To find the  $\Delta\boldsymbol{\theta}$  that minimizes  $\Psi(\boldsymbol{\theta})$ , we equate its gradient with respect to  $\Delta\boldsymbol{\theta}$  to zero:

$$\frac{\partial}{\partial \Delta\boldsymbol{\theta}} \Psi(\boldsymbol{\theta}) = \left[ \frac{\partial \Phi}{\partial \boldsymbol{\theta}} \right]_{\boldsymbol{\theta}_0} + \left[ \frac{\partial^2 \Phi}{\partial \boldsymbol{\theta}^2} \right]_{\boldsymbol{\theta}_0} \Delta\boldsymbol{\theta} = 0$$

---

<sup>1</sup>For the purposes of our analyses, we consider  $\mathbf{Q}$  to be diagonal.

To find the stationary point  $\boldsymbol{\theta}_1$ , the previous equation can be rearranged as follows:

$$\left[ \frac{\partial^2 \Phi}{\partial \boldsymbol{\theta}^2} \right]_{\boldsymbol{\theta}_0} (\boldsymbol{\theta}_1 - \boldsymbol{\theta}_0) = - \left[ \frac{\partial \Phi}{\partial \boldsymbol{\theta}} \right]_{\boldsymbol{\theta}_0} \quad (4.3)$$

If the inverse of the Hessian exists,  $\boldsymbol{\theta}_1$  is given by:

$$\boldsymbol{\theta}_1 = \boldsymbol{\theta}_0 - \left[ \frac{\partial^2 \Phi}{\partial \boldsymbol{\theta}^2} \right]_{\boldsymbol{\theta}_0}^{-1} \cdot \left[ \frac{\partial \Phi}{\partial \boldsymbol{\theta}} \right]_{\boldsymbol{\theta}_0} \quad (4.4)$$

If the Hessian is positive definite,  $\Psi(\boldsymbol{\theta}_1) < \Psi(\boldsymbol{\theta}_0)$ , making  $\boldsymbol{\theta}_1$  a reasonable estimate of the minimizing value of  $\Phi(\boldsymbol{\theta})$ ; hence  $\boldsymbol{\theta}_1$  assumes the role of  $\boldsymbol{\theta}_0$  in the next iteration [25]. The iterations continue until some exit criteria are satisfied, which usually include setting thresholds on the cost function value, and on the distance between two consecutive parameter estimates. Refinements are possible, where one picks  $\boldsymbol{\theta}_1$  in the direction suggested by Equation 4.4, but taking a scaled version of the indicated step. However, we use only the basic method here.

For the cost function defined by Equation 4.1, the gradient is given as:

$$\left[ \frac{\partial \Phi}{\partial \boldsymbol{\theta}} \right] = \mathbf{J}^T \mathbf{Q} \mathbf{r}(\boldsymbol{\theta}) \text{ where } J_{ij} = \frac{\partial r_i(\boldsymbol{\theta})}{\partial \theta_j} = \frac{\partial \hat{y}_i(\boldsymbol{\theta})}{\partial \theta_j} \quad (4.5)$$

$\mathbf{J} \in \mathbb{R}^{n \times m}$  is the Jacobian matrix of the error vector with respect to the parameter vector. The elements of the Hessian matrix  $\mathbf{H} \in \mathbb{R}^{m \times m}$ , are given by:

$$H_{ij} = \frac{\partial^2 \Phi}{\partial \theta_i \partial \theta_j} = (\mathbf{J}^T \mathbf{Q} \mathbf{J})_{ij} + \sum_{l=1}^n \sum_{p=1}^n Q_{lp} \cdot r_p \cdot \frac{\partial^2 r_l}{\partial \theta_i \partial \theta_j}$$

In the presence of small residuals, the Gauss-Newton approximation to the Hessian states that the terms containing the residuals can be ignored, thus giving the following approximation:

$$H_{ij} = \frac{\partial^2 \Phi}{\partial \theta_i \partial \theta_j} \approx (\mathbf{J}^T \mathbf{Q} \mathbf{J})_{ij}$$

Substituting the expressions for the cost function derivatives into Equation 4.3, we obtain

the following equation for the parameter estimate updates:

$$\mathbf{J}^T \mathbf{Q} \mathbf{J} \cdot (\boldsymbol{\theta}_{i+1} - \boldsymbol{\theta}_i) = -\mathbf{J}^T \mathbf{Q} \cdot \mathbf{r} \quad (4.6)$$

The Gauss-Newton approximation reduces the nonlinear least squares optimization problem to a series of linear least squares equations that are solved iteratively.

Let  $\mathbf{R}$  represent the Hessian matrix or its Gauss-Newton approximation. To illustrate the problem of ill-conditioning, we follow the reasoning presented by Heldt [7], based on the arguments of Burth and co-workers [26]. If the matrix  $\mathbf{R}$  is rank-deficient, then it is singular, with at least one of its eigenvalues at zero, and its column space does not span the entire  $\mathbb{R}^m$  space. Consequently, the parameter update vector can be arbitrarily varied in the direction of any  $\boldsymbol{\vartheta}$  that belongs to the null-space of  $\mathbf{R}$ , without affecting the error criterion:

$$\mathbf{R} \cdot (\boldsymbol{\theta}_{i+1} - \boldsymbol{\theta}_i + \boldsymbol{\vartheta}) = \mathbf{R} \cdot (\boldsymbol{\theta}_{i+1} - \boldsymbol{\theta}_i) + \mathbf{R} \cdot \boldsymbol{\vartheta} = \mathbf{R} \cdot (\boldsymbol{\theta}_{i+1} - \boldsymbol{\theta}_i) = -\mathbf{J}^T \mathbf{Q} \mathbf{r}$$

Thus, if  $\mathbf{R}$  is singular, then the model parameters are not uniquely determinable from the available observation data; such an estimation problem is said to be over-parameterized.

Typically though,  $\mathbf{R}$  is not exactly singular, but nearly so, with its largest singular value much greater than its smallest. Nearness to singularity is measured by the condition number,  $\kappa(\mathbf{R})$ , which, for real and symmetric matrices, is given by the ratio of the largest to the smallest eigenvalues. This nearness to singularity gives an ill-conditioned problem, in which small numerical errors or noise in the underlying data can radically modify the solution.

To overcome the problem of ill-conditioning, we turn to the subset selection algorithm that determines which parameters should be discarded from the estimation formulation in order to improve the conditioning of the system.

### 4.1.2 Subset Selection

Subset selection aims to identify the parameter axes that lie closest to the ill-conditioned directions of the Hessian matrix [26]. As the error criterion varies very slowly in the direction

of ill-conditioned parameter axes, we choose to fix the corresponding parameters at prior values while the estimation process is carried out with a reduced-order formulation. Though fixing the ill-conditioned parameters introduces some bias into the estimates, the effect of the bias is offset by the improved reliability with which the rest of the parameters are estimated.

The number of well-conditioned parameters is determined from the structure of the Hessian eigenspectrum. If the Hessian eigenspectrum contains  $\rho$  large eigenvalues and  $m - \rho$  small ones, then this indicates that the Hessian has a numerical rank of  $\rho$ , and that only the corresponding  $\rho$  parameters should be included in the estimation formulation. The reduced-order estimation problem involves the use of reduced dimension Jacobian and Hessian matrices, indicated by  $\mathbf{J}_\rho$  and  $\mathbf{H}_\rho$  respectively.  $\mathbf{J}_\rho$  contains  $\rho$  columns of the original Jacobian matrix that are strongly independent, which results in a small condition number for the corresponding  $\mathbf{H}_\rho$ .

The following procedure, based on the work of Vélez-Reyez [27] and as described in Burth and co-workers [26], outlines the algorithm for subset selection:

1. Using an initial parameter vector estimate  $\hat{\boldsymbol{\theta}}_0$ , calculate the eigendecomposition of  $\mathbf{H}(\hat{\boldsymbol{\theta}}_0)$ :  $\mathbf{H} = \mathbf{V}\boldsymbol{\Lambda}\mathbf{V}$ , such that the eigenvalues in  $\boldsymbol{\Lambda}$  are in descending order.
2. Determine  $\rho$  such that the first  $\rho$  eigenvalues of  $\mathbf{H}$  are much larger than the remaining  $m - \rho$  ones.
3. Partition  $\mathbf{V} = [\mathbf{V}_\rho \mathbf{V}_{m-\rho}]$ .
4. Determine a permutation matrix  $\mathbf{P}$  by constructing a  $QR$  decomposition with column-pivoting for  $\mathbf{V}_\rho^T$  i.e. determine  $\mathbf{P}$  such that:

$$\mathbf{V}_\rho^T \cdot \mathbf{P} = \mathbf{Q} \cdot \mathbf{R}$$

where  $\mathbf{Q}$  is an orthogonal matrix and the first  $\rho$  columns of  $\mathbf{R}$  form an upper triangular matrix.

5. Use  $\mathbf{P}$  to re-order the parameter vector  $\boldsymbol{\theta}$  according to  $\tilde{\boldsymbol{\theta}} = \mathbf{P}^T \boldsymbol{\theta}$ .

6. Partition  $\tilde{\boldsymbol{\theta}} = [\tilde{\boldsymbol{\theta}}_\rho^\top \tilde{\boldsymbol{\theta}}_{m-\rho}^\top]^\top$ , where  $\tilde{\boldsymbol{\theta}}_\rho^\top$  contains the first  $\rho$  elements of  $\tilde{\boldsymbol{\theta}}$ . Fix  $\tilde{\boldsymbol{\theta}}_{m-\rho}$  at prior estimate  $\hat{\tilde{\boldsymbol{\theta}}}_{m-\rho}$ .
7. Compute  $\hat{\tilde{\boldsymbol{\theta}}}$  by solving the reduced-order problem  $\hat{\tilde{\boldsymbol{\theta}}} = \arg \min_{\tilde{\boldsymbol{\theta}}} \Phi(\tilde{\boldsymbol{\theta}})$  subject to  $\hat{\tilde{\boldsymbol{\theta}}}_{m-\rho} = \tilde{\boldsymbol{\theta}}_{m-\rho}$ .

### 4.1.3 Jacobian Calculation and Scaling

Although methods exist to compute the Jacobian matrix analytically, the large number of parameters and output variables warrants the use of a finite-difference approximation. We used a two-sided finite difference method with a step-size of 4% of the nominal parameter values. Equation 4.7 illustrates the finite-difference approximation:

$$\mathbf{J}(\boldsymbol{\theta}) = \frac{\partial \hat{\mathbf{y}}(\boldsymbol{\theta})}{\partial \boldsymbol{\theta}} \approx \frac{\hat{\mathbf{y}}(\boldsymbol{\theta} + \Delta \boldsymbol{\theta}) - \hat{\mathbf{y}}(\boldsymbol{\theta} - \Delta \boldsymbol{\theta})}{2\Delta \boldsymbol{\theta}} \quad (4.7)$$

As the input parameter values span several orders of magnitude and have different units of measurement, the columns of the Jacobian need to be normalized. Normalizing the columns would lead to meaningful comparisons between the column norms, which represent the strengths with which perturbations in parameters affect the entire observable output. Moreover, the Jacobian rows also need to be normalized, as they too span several orders of magnitude. The observable output consists of single-cycle waveforms of ABP, CVP, and PAP signals, which vary greatly in magnitude, not only relative to each other, but also within a signal itself during a cardiac cycle. In order to prevent the residual errors in any one output variable from dominating, which can cause a loss of information contained in the rest of the residuals, the rows of the Jacobian need to be normalized. Furthermore, the subset selection algorithm is not scaling-invariant [28], hence meaningful scalings of the Jacobian can be used to improve the curvature of the error-criterion surface and thereby help in identifying the well-conditioned parameters.

We applied two different kinds of scalings to the Jacobian. The first scheme, which we shall refer to as nominal scaling, scaled the columns of the Jacobian by the nominal

parameter values (correspondingly scaling the parameter variations by the inverses of the nominal parameter values), and scaled the rows by some characteristic output values, which in our case, were the nominal output values. Such a scaling leads the columns of the Jacobian to contain percentage changes in observable output as a response to percentage changes in parameter values.

The second scheme, which we shall refer to as range scaling, scaled the columns by the dynamic ranges of the parameters instead of the nominal values<sup>2</sup>. Subsequently, the rows were scaled so that they would have a norm of unity, thereby preventing the residual errors in any one output variable from dominating. Such a scaling scheme gives a sense of how the parameters affect normalized output when they are perturbed as a percentage of their dynamic ranges.

In the context of solving the nonlinear least squares problem, row scaling leads to the weighting of residuals, which is handled by the  $\mathbf{Q}$  matrix in Equation 4.1. Column scaling, however, needs to be explicitly added, and modifies the parameter update equation (see Equation 4.6) to the following:

$$\mathbf{M}\mathbf{J}^T\mathbf{Q}\mathbf{J}\mathbf{M}\hat{\mathbf{p}} = -\mathbf{M}\mathbf{J}^T\mathbf{Q}\mathbf{r} \quad (4.8)$$

where  $\mathbf{M} \in \mathbb{R}^{m \times m}$  is a diagonal matrix of column scalings and  $\hat{\mathbf{p}} = \mathbf{M}^{-1} \cdot (\boldsymbol{\theta}_{i+1} - \boldsymbol{\theta}_i)$ . The above equation is obtained by replacing each occurrence of  $\mathbf{J}$  in Equation 4.6 with its column scaled version  $\mathbf{J}\mathbf{M}$ . Equation 4.8 can be re-written as follows:

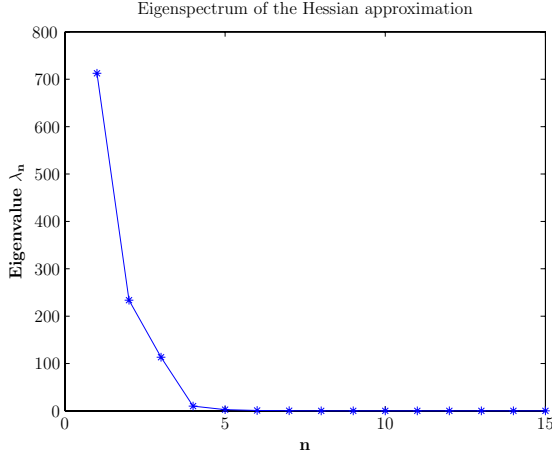
$$(\sqrt{\mathbf{Q}}\mathbf{J}\mathbf{M})^T \cdot (\sqrt{\mathbf{Q}}\mathbf{J}\mathbf{M}) \cdot \hat{\mathbf{p}} = -(\sqrt{\mathbf{Q}}\mathbf{J}\mathbf{M})^T \cdot \tilde{\mathbf{r}} \quad (4.9)$$

where  $\tilde{\mathbf{r}} = \sqrt{\mathbf{Q}}\mathbf{r}$ . The Gauss-Newton approximation of the Hessian using the scaled version of the Jacobian is therefore given as:

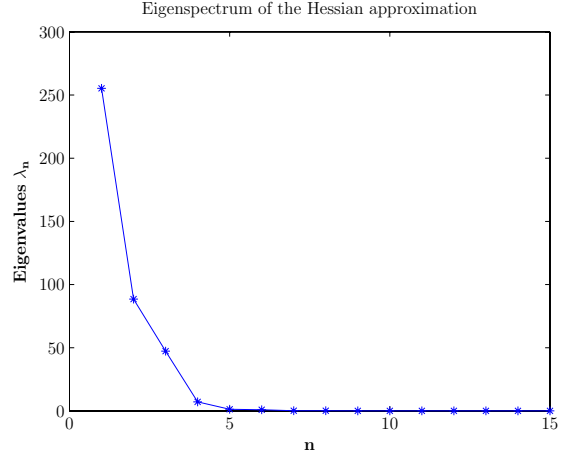
$$\mathbf{H} \approx (\sqrt{\mathbf{Q}}\mathbf{J}\mathbf{M})^T \cdot (\sqrt{\mathbf{Q}}\mathbf{J}\mathbf{M}) \quad (4.10)$$

---

<sup>2</sup>See Appendix B for a list of all the independent parameters of the model and their range of values.



(a) Eigenvalue spectrum of the Hessian approximation under the nominal scaling scheme.



(b) Eigenvalue spectrum of the Hessian approximation under the range scaling scheme.

Figure 4-1: Eigenvalue spectrum of the Hessian approximation under the two different scaling schemes applied.

Table 4.1: Parameters identified as being well-conditioned by the subset selection algorithm.

Parameter no.	Nominal Scaling	Range Scaling
1	Distending blood volume (DBV)	Right end-diastolic compliance ( $C_r^{ed}$ )
2	Peripheral Resistance ( $R_a$ )	Peripheral Resistance ( $R_a$ )
3	Right end-diastolic compliance ( $C_r^{ed}$ )	Distending blood volume (DBV)

#### 4.1.4 Application of the Subset Selection Algorithm

We applied the subset selection algorithm to the problem of estimating cardiovascular parameters using single-cycle waveforms of ABP, CVP, and PAP signals. Figure 4-1 shows a plot of the eigenvalue spectrum of the Hessian approximation under the two different scaling schemes applied. The Hessian approximation has three strong eigenvalues under both scalings, indicating the existence of three well-conditioned or “active” parameters. Table 4.1 lists the parameters identified as being well-conditioned under the two scaling schemes. Although the sequence of the active parameters is different, both scalings lead to the selection of the same three parameters. Thus, in our application, the type of scaling did not affect the solution of the subset-selection algorithm.

### 4.1.5 Description of the Estimation Problem

Guided by the results of the subset selection algorithm, we attempted to estimate the well-conditioned parameters using single-cycle waveforms of ABP, CVP, and PAP signals, in both steady-state and transient conditions. We used the built-in Matlab routine, ‘lsqnonlin’, to apply the Gauss-Newton nonlinear least squares optimization in an effort to recover the parameters. The rows of the Jacobian were scaled by the target output values and the columns of the Jacobian were scaled by nominal parameter values. As we are interested in judging the performance of the estimation algorithm, we must know the true values of the underlying parameters. We therefore used our computational model to produce synthetic data, which was then treated as “measurements” to which we applied the estimation algorithm.

For the estimation problem using steady-state data, we generated target data using randomized parameters. Each parameter,  $\theta_i$ , was perturbed using a Gaussian distribution  $\sim N(\theta_i^0, 10\%\theta_i^0)$ , where  $\theta_i^0$  is the nominal parameter value. In an attempt to investigate the benefit of using subset selection, this target data was used in two different estimation schemes: one in which only the active parameters were estimated while the rest were fixed at their nominal values, and one in which all the parameters were estimated.

Next, we generated transient data by simulating several cases of hemorrhage that lasted for 30 minutes each. The data was generated using randomized parameters (same randomization scheme as before), and each waveform was perturbed with additive noise from a Gaussian distribution  $\sim N(0, 1.7\%m_i)$ , where  $m_i$  refers to the cycle-average of the waveform. For each hemorrhage case, the active parameters were estimated six times at uniform time intervals.

## 4.2 Results

### 4.2.1 Estimation using Steady-State Waveform Data

Table 4.2 summarizes the relative errors incurred in estimating the active parameters from steady-state waveform data under two different estimation formulations:

Table 4.2: Estimation error statistics for the active parameters under two schemes: estimating only the active parameters with the ill-conditioned ones fixed at their nominal values, and estimating all the model parameters.

Active parameter	Estimating only the active parameters		Estimating all the parameters	
	Mean	St. deviation	Mean	St. deviation
<b>DBV</b>	6.35%	4.77%	13.30%	11.39%
$R_a$	7.38%	5.78%	16.12%	10.20%
$C_r^{ed}$	7.07%	7.11%	15.33%	10.66%

- Estimating only the active parameters while the rest are fixed at their nominal values.
- Estimating all the model parameters.

We observe that reducing the dimensionality of the estimation problem improves the mean reliability of the active parameter estimates by more than 50%. Figure 4-2 illustrates the plots of the estimated versus actual well-conditioned parameters for the individual runs of the reduced dimensionality estimation experiment.

The estimation errors that occur when recovering the reduced set of parameters are mainly due to the bias introduced by fixing the values of the ill-conditioned parameters. In an attempt to reduce the error between model output and observed data, the estimation algorithm distorts the active parameter estimates in order to compensate for the fixing of the ill-conditioned parameters. As such, large deviations from nominal value in any ill-conditioned parameter that has similar effect on model output as any one of the active parameters (or their combination), would lead to significant estimation errors.

In our estimation experiments, large deviations in the venous compliance ( $C_v$ ) value from its nominal value were seen to lead to significant errors in DBV estimates, indicating that these two parameters affect the model output in a similar fashion. This fact was verified mathematically by analyzing the Jacobian matrix. Recall that the columns of the Jacobian consist of  $\frac{\partial \mathbf{y}}{\partial \theta_j}$  (see Equation 4.5), which is a measure of parametric sensitivity for a particular parameter  $\theta_j$ . The columns of the Jacobian therefore indicate how the model

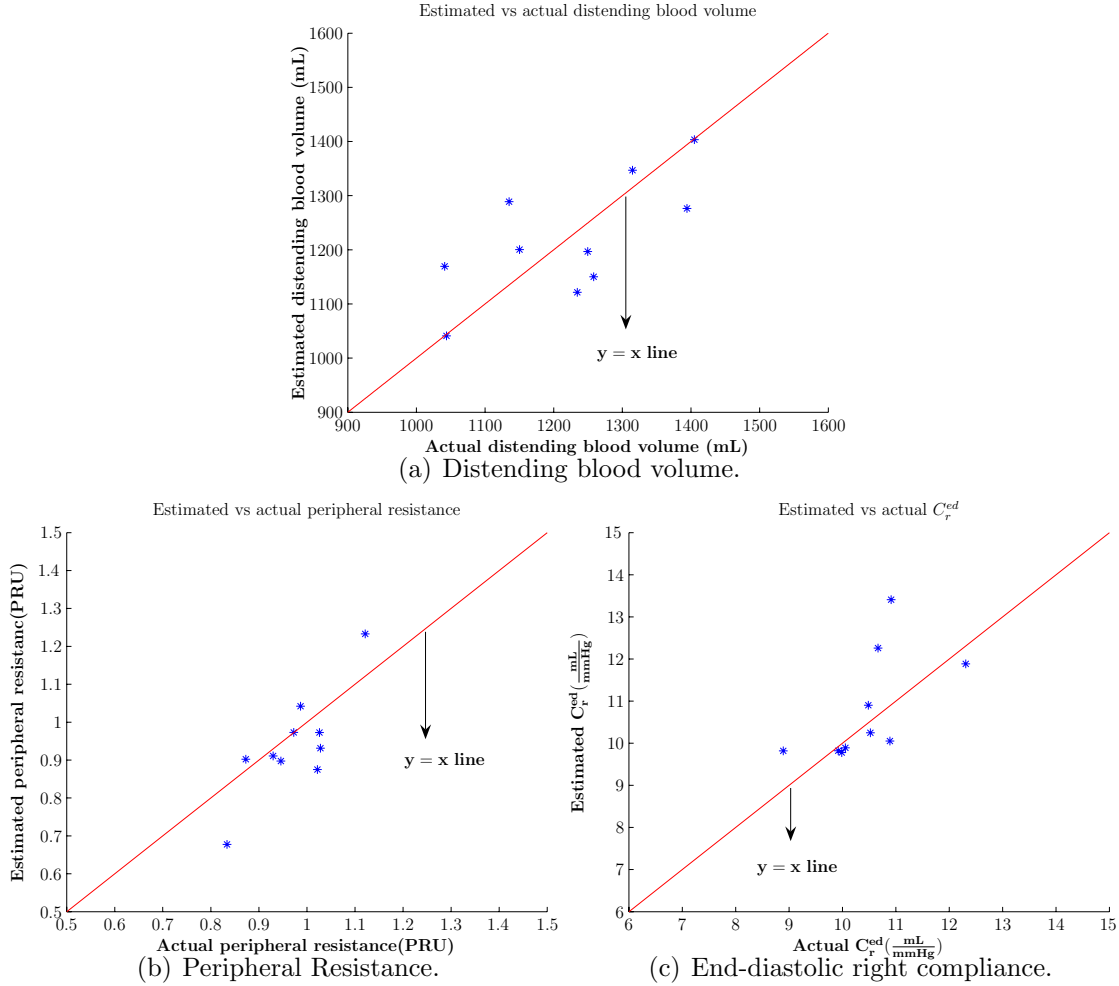


Figure 4-2: Estimated active parameters recovered using steady-state waveform data vs actual active parameters.

output changes in  $\mathbb{R}^n$  space in response to changes in parameter values. If any of the columns of the Jacobian are collinear, then the corresponding parameters affect the model output in the same direction within the  $\mathbb{R}^n$  space. It turns out that the columns of the Jacobian corresponding to  $C_v$  and DBV ( $\frac{\partial \mathbf{y}}{\partial \theta_{DBV}}, \frac{\partial \mathbf{y}}{\partial \theta_{C_v}}$ ) are almost collinear, with the angle between them being  $0.99\pi$  radians. Hence, changes in these two parameter values can have an almost indistinguishable effect on the model output, with opposite signs. In fact, a straightforward explanation exists for this observation. For a given venous pressure and DBV, a decrease in  $C_v$  would decrease the venous volume and hence would increase the blood volume in the

Table 4.3: Estimation error statistics for the active parameters with  $C_v$  and  $C_l^{ed}$  fixed at their actual values.

Active parameter	Mean	St. deviation
<b>DBV</b>	1.06%	0.66%
$R_a$	3.14%	1.42%
$C_r^{ed}$	4.14%	7.11%

other compartments. Thus, a decrease in  $C_v$  would lead to similar changes in model output as an increase in DBV.

Similarly, poor estimates of  $R_a$  and  $C_r^{ed}$  were correlated to large deviations in the left end-diastolic compliance ( $C_l^{ed}$ ) value from its nominal value. Analysis of the Jacobian revealed that  $\frac{\partial \mathbf{y}}{\partial \theta_{C_l^{ed}}}$  almost lies in the plane spanned by  $\frac{\partial \mathbf{y}}{\partial \theta_{R_a}}$  and  $\frac{\partial \mathbf{y}}{\partial \theta_{C_r^{ed}}}$ : the angle between  $\frac{\partial \mathbf{y}}{\partial \theta_{C_l^{ed}}}$  and its projection on the plane spanned by  $\frac{\partial \mathbf{y}}{\partial \theta_{R_a}}$  and  $\frac{\partial \mathbf{y}}{\partial \theta_{C_r^{ed}}}$  is  $0.12\pi$  radians. Thus, deviations in  $C_l^{ed}$  values can somewhat be compensated for by changes in the values of  $R_a$  and  $C_r^{ed}$ .

To validate our analysis of major contributors of bias, we re-ran our estimation experiments with  $C_v$  and  $C_l^{ed}$  fixed at their *actual* values instead of their *nominal* ones. Table 4.3 summarizes the estimation errors incurred under this scheme. We observe that the mean estimation error for DBV was reduced by more than 80%, whereas the mean errors for the other two parameters were reduced by more than 40% each. These results confirm our analysis that uncertainties in the values of  $C_v$  and  $C_l^{ed}$  can lead to significant errors in estimating the active parameters.

## 4.2.2 Estimation using Transient Waveform Data (Hemorrhage Data)

In tracking the active parameters through time during a transient, there is an opportunity to overcome some of the bias introduced due to the unknown values of the ill-conditioned parameters. For example, during a hemorrhage, DBV is constantly changing, hence estimating *change* in DBV rather than *actual* DBV would remove some of the bias in the estimate. Figure 4-3 illustrates the plot of estimated versus actual change in DBV for all the hem-

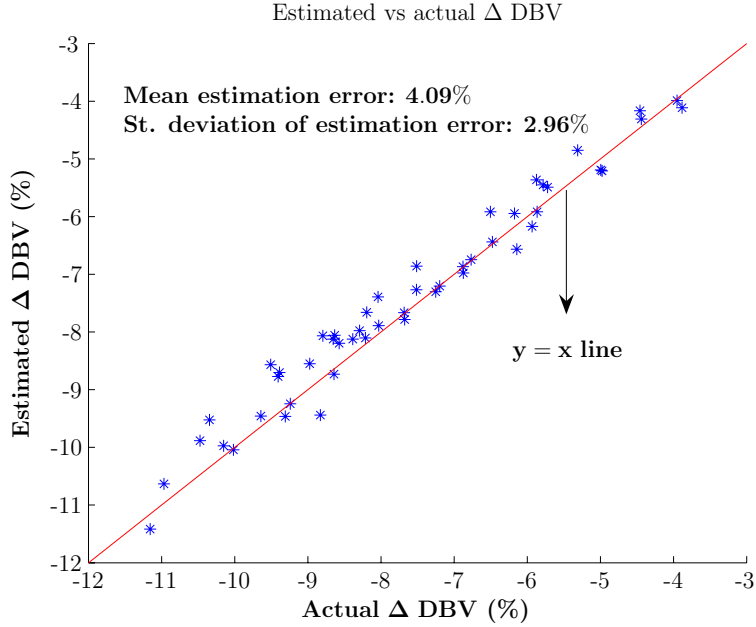


Figure 4-3: Estimated vs actual change in DBV for all the simulated hemorrhage cases analyzed.

orrhage cases<sup>3</sup>. The estimation error statistics are overlaid on the plot. The estimates are reasonably close to the actual change in DBV, with a mean error of less than 5%.

Figure 4-4a shows the plot of estimated vs actual  $R_a$  for all the hemorrhage cases. As the values of  $R_a$  are small, and the values of changes in  $R_a$  are even smaller, the numerical errors associated with the estimates of either  $R_a$ , or changes in  $R_a$ , are large and unrepresentative of the quality of the estimates. Nevertheless, a strong correlation exists between the estimated and actual values, indicated by their almost linear relationship in the plot. In order to exploit the observed correlation in an attempt to improve the estimation, we performed a first-point calibration. As measures of cardiac output (CO) are occasionally available in the ICU, they can be used in conjunction with the mean ABP and CVP measurements to calculate  $R_a$ . We assume that for each hemorrhage case, the initial value of peripheral resistance,  $R_a^{k,i}$ , is known, where  $k$  represents an individual hemorrhage case. The ratio of the initial peripheral resistance value to its estimated value is used to determine a gain factor,  $g^k$ , which scales

---

<sup>3</sup>Recall that for each hemorrhage case, the active parameters were estimated six times at uniform time intervals.

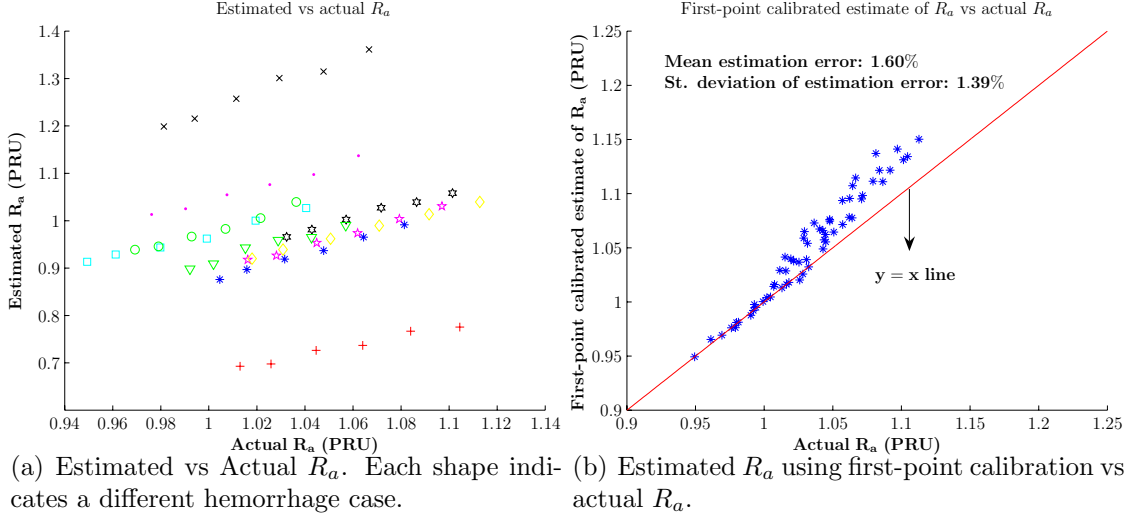


Figure 4-4: Estimated vs actual  $R_a$  for all the hemorrhage cases analyzed.

all subsequent estimates of  $R_a$  during the hemorrhage case  $k$ . This scaling procedure, where the gain factor is constant and calculated based on the first estimate, is known as first-point calibration. Figure 4-4b shows the estimation results for  $R_a$  obtained with first-point calibration. The resulting estimation errors are small, with the mean error standing at less than 2%. However, the estimates exhibit a deviating trend from the  $y = x$  line, indicating the need for re-calibration as often as possible.

For each hemorrhage simulation, the value of  $C_r^{ed}$  remained constant and did not change during the hemorrhage; therefore, we were unable to exploit the bias removal techniques used previously for the estimates of DBV and  $R_a$ . Figure 4-5 illustrates the results for the  $C_r^{ed}$  estimates. As multiple  $C_r^{ed}$  estimates were obtained for every case, each value on the plot represents the mean value of the estimates for each case. The estimation errors for  $C_r^{ed}$  are relatively higher compared to those of DBV and  $R_a$ , however, the estimates are still quite reasonable, with mean error less than 8.0%.

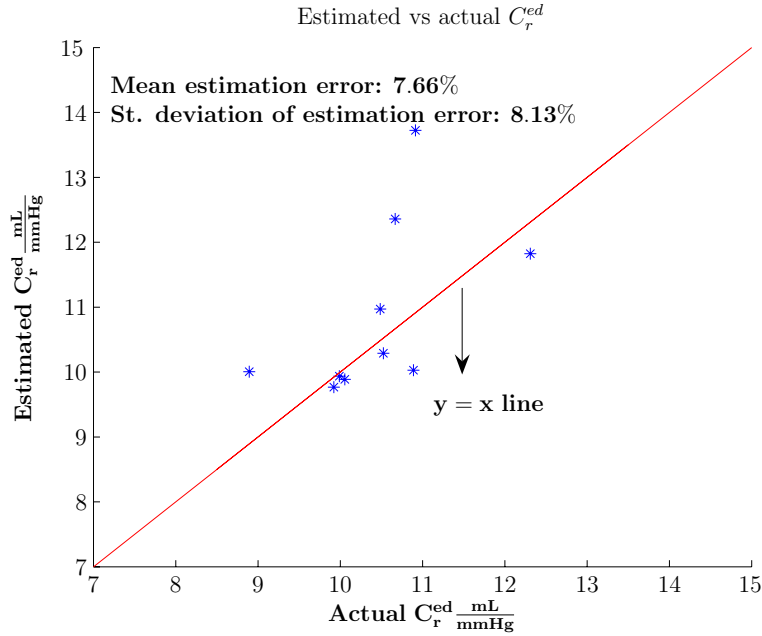


Figure 4-5: Estimated  $C_r^{ed}$  vs actual  $C_r^{ed}$  for the hemorrhage cases.

### 4.3 Concluding Remarks

In this chapter, we focused on parameter estimation using waveform data. We employed a nonlinear least squares optimization technique to recover the model parameters and we used subset selection to improve the conditioning of the problem. We observed that the reduced dimensionality estimation problem improved the reliability of the estimated parameters substantially. Furthermore, the estimation algorithm showed promising results when tested on simulated steady-state and transient data.



# Chapter 5

## Parameter Tracking using Beat-to-Beat Averaged Data

In the previous chapter, we investigated the use of subset selection to reduce the dimensionality of the estimation problem. The reduced dimensionality problem increased the reliability of the estimated parameters and outperformed the full-fledged estimation of all the model parameters. In this chapter, we focus on another method of dimensionality reduction which results from a simplifying assumption.

Depending on the disease condition, only a selected few parameters change in time as the disease state progresses. In this case, it is not required to estimate all the parameter values; estimating only the disease-dependent, physiologically significant parameters would suffice to reveal information about patient state. If we assume prior knowledge of initial parameter values, we need to track only the physiologically significant parameters in time, and thus the dimensionality of the estimation problem is reduced.

We carry out our investigation in the context of a real patient hemorrhage case. As we are interested in tracking parameters over transients spanning long periods of time, we use beat-to-beat averaged data for estimation instead of waveform data. The averaged data sufficiently represents long-term transients, and hence it is not necessary to use the high-resolution waveform data. Though we are using a pulsatile computational model, the model

output can be averaged to represent beat-to-beat trend data.

We begin by providing a brief patient history and description of the data available. Next, we outline the estimation algorithm and highlight some issues faced during parameter estimation. Subsequently, we present the results of the algorithm and provide concluding remarks.

## 5.1 Brief Patient History

The patient is an 83 year old female who was admitted to the ICU after falling at her nursing home. She complained of pains in her left knee and hip; an x-ray revealed that she had a loose acetabular shell and possibly a loose femoral head. As the patient was on anticoagulants due to a previous aortic valve replacement, it was decided not to take any immediate surgical action, but wait for the anticoagulant effects to wear off.

During the waiting period, the patient suddenly developed pain in her lower right abdomen. Upon further examination, a 6x6 cm mass was found in the right abdomen caused by a lumbar artery bleed. The patient was then transferred to interventional radiology where the bleed was embolized. After the embolization procedure, the patient was returned to the ICU where she made a full recovery with the help of fluid resuscitation and vasoactive drugs.

## 5.2 Patient Data for Parameter Tracking

For purposes of parameter tracking, we consider a time-period of approximately 50 minutes pre-embolization, when the patient vital statistics displayed some interesting characteristics. Figure 5-1 shows a plot of the patient heart rate and blood pressure during that period. The heart rate stays relatively constant at around 130 beats/min, indicating that the control system may have saturated, while the blood pressure goes through significant transients.

The only other relevant information available for this time-period consists of clinical intervention data regarding medication and fluid resuscitation. This information is necessary for determining the causes for the observed changes in patient state; however, it may lack

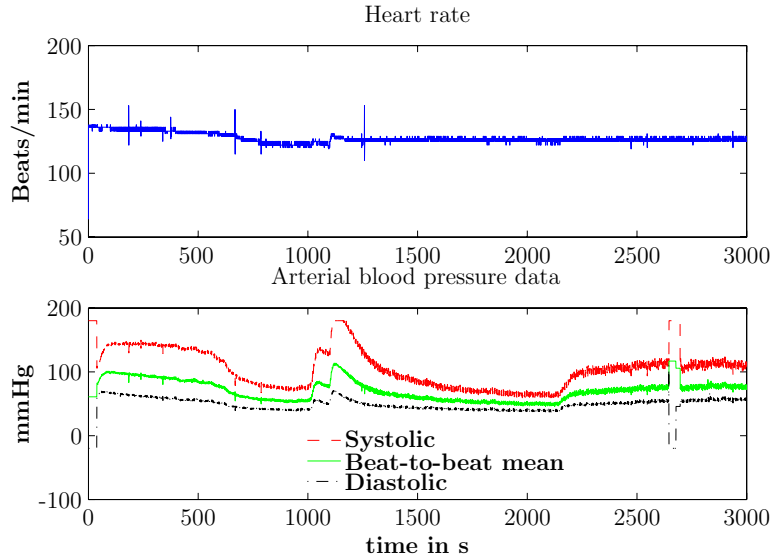


Figure 5-1: Heart rate (upper panel) and arterial blood pressure (lower panel) patient data.

time accuracy. Information regarding changes in medication and their doses is usually hand-recorded afterwards by the administering nurse, using approximate, rounded-off time-stamps. Therefore, the times at which the changes actually occur may differ from the recorded ones. Moreover, fluid resuscitation information is only recorded on an hourly basis, hence the exact time of a fluid bolus administration is not available. Furthermore, hand-recorded information is often prone to errors and omissions.

Figure 5-2 shows the time-series plot of a vasopressor drug called Levophed (the beat-to-beat averaged ABP data is also shown so that the medication data can be put into perspective). Vasopressors serve to increase blood pressure by constricting the arterioles. Levophed was the only drug whose dosage changed during this time period. The doses of the rest of the administered drugs remained constant not only within this time-period, but also in its neighborhood; hence these other medications were not considered to be significant contributing factors to the patient’s physiology for this time portion. Although there are no recorded fluid boluses administered during this time-period, our in-house medical experts believe that absence to be a recording artifact. Expert medical opinion suggests that the

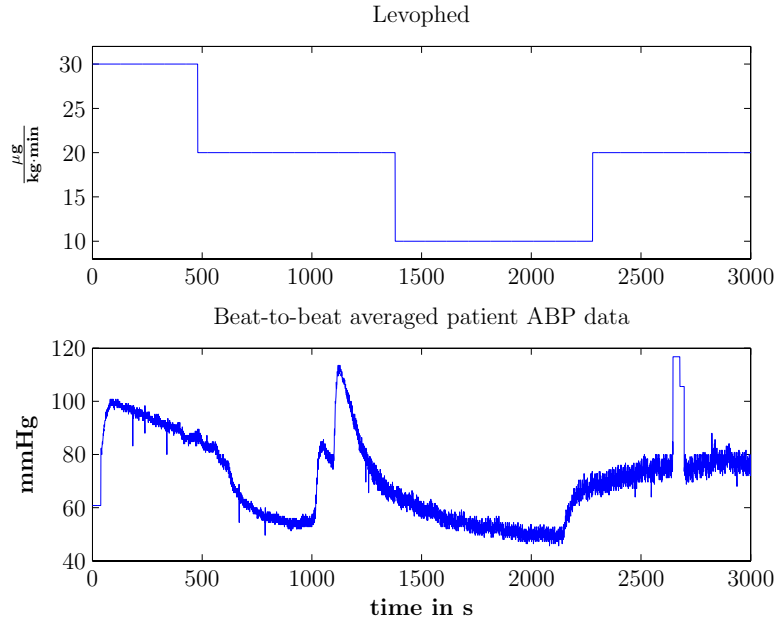


Figure 5-2: Levophed administration (top panel) and beat-to-beat averaged patient ABP data (bottom panel).

rises in blood pressure at around  $t=1000$ s, and again at around  $t=1100$ s, are results of fluid bolus administrations.

The information available is clearly not sufficient to derive, or even get an idea of, the actual values of the underlying physiological parameters. In this case, there is no way to judge the performance of a parameter estimation algorithm, as the quality of the estimates cannot be determined. To overcome this problem, we adopted an approach whereby we first used our cardiovascular model to simulate data that matched the patient ABP data, and then we used the simulated data to perform estimation. Using this methodology, the values of the model parameters are known, so the performance of the estimation algorithm can be judged quantitatively.

### 5.3 Simulating Patient Data

Given anthropometric measurements of a patient, allometric scaling can be applied to nominal parameter values to obtain a set of parameters that are more representative of a particular

individual [7]. However, anthropometric measurements for this patient were not available, hence we used nominal values for all parameters except heart rate and distending blood volume (DBV). The patient heart rate data is available (see Figure 5-1) and is considered to be relatively constant; the heart rate parameter was therefore fixed at 130 beats/min in our simulation. As this is a case of hemorrhage, we reduced the initial DBV until the simulator output matched the initial patient ABP data.

The model used to simulate patient data included a leak on the arterial side to model bleeding, and it had the capability to incorporate a time-varying peripheral resistance ( $R_a$ ). These changes add two new parameters to the model: bleeding rate and rate of change of  $R_a$ . To capture the dynamics displayed by blood pressure data, we modified bleeding rate and rate of change of  $R_a$  following some reasonable assumptions based on the the patient pathology and nurse's notes. The changes in  $R_a$  were guided by Levophed medication; whenever Levophed dose went down, we reduced  $R_a$  and vice versa<sup>1</sup>. The partial recoveries in blood pressure at times  $t=1000s$  and  $t=1100s$  were simulated by administrating fluid boluses. Figure 5-3 shows a plot of simulated and actual beat-to-beat averaged blood pressure data. The simulated plot has regions marked 1-10 which correspond to the following actions taken to simulate them:

- 1) 0 – 500s: Bled @ 0.76 mL/s.
- 2) 500 – 700s: Bled @ 0.76 mL/s +  $R_a$  ramped down from 1.1 to 0.8 PRU.
- 3) 700 – 1010s: Bled @ 0.76 mL/s.
- 4) 1010 – 1040s: Bled @ 0.76 mL/s + Bolus of 470 mL administered as a ramp function.
- 5) 1040 – 1100s: Bled @ 0.6 mL/s.
- 6) 1100 – 1120s: Bled @ 0.6 mL/s + Bolus of 570 mL administered as a ramp function.

---

<sup>1</sup>It was taken into account that the time recordings for Levophed doses may lag behind the actual times. For example, the effects of recorded dose changes at around  $t=1400s$ , and again at around  $t=2300s$ , seem to occur prior to the recorded times, indicating that the medication recordings may have followed the actual times at which the changes occurred. See Appendix C for an attempt to validate the assumptions made regarding changes in peripheral resistance.

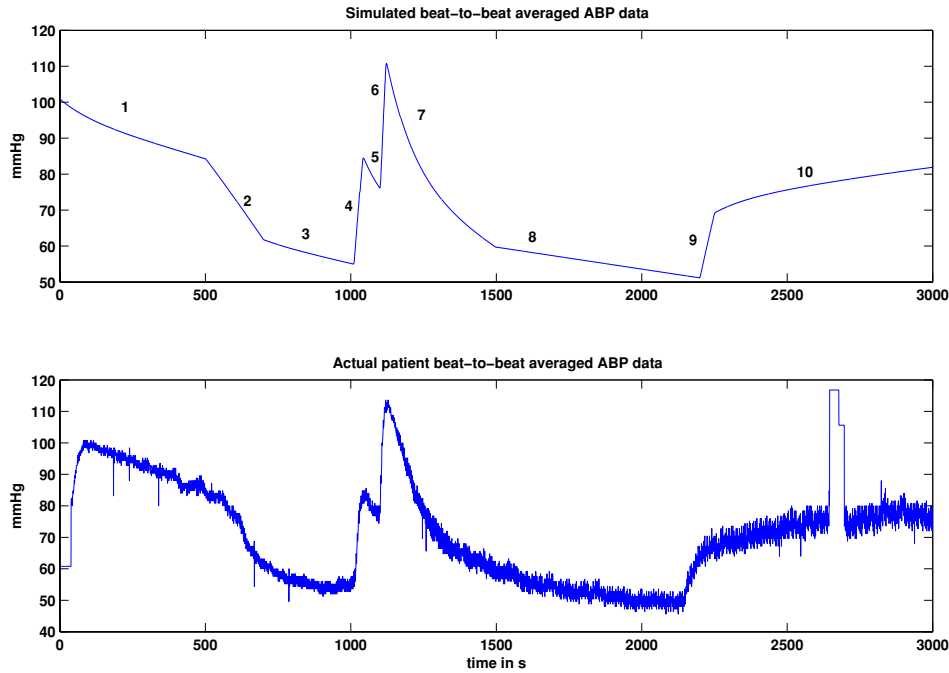


Figure 5-3: Simulated beat-to-beat averaged ABP data (top panel) and actual patient ABP data (bottom panel).

- 7) 1120 – 1500s: Bled @ 0.85 mL/s +  $R_a$  ramped down from 0.8 to 0.65 PRU.
- 8) 1500 – 2200s: Bled @ 0.6 mL/s.
- 9) 2200 – 2250s: Bled @ 0.25 mL/s +  $R_a$  ramped up from 0.65 to 0.95 PRU.
- 10) 2250 – 3000s: Bled @ 0.25 mL/s +  $R_a$  ramped up from 0.95 to 1.2 PRU.

The simulated ABP data follows the transients exhibited by the real patient data reasonably well. Next, we added noise to each simulated point using a Gaussian distribution,  $\sim N(0, 2\%p_i)$ , where  $p_i$  refers to the  $i^{th}$  point. Figure 5-4 shows a plot of the noise-corrupted simulated ABP data and the actual patient data. We observe that the noisy simulated data closely follows the real patient data, and therefore the simulated data is said to be representative of the actual. Henceforth, the simulated data will be referred to as pseudo-patient data.

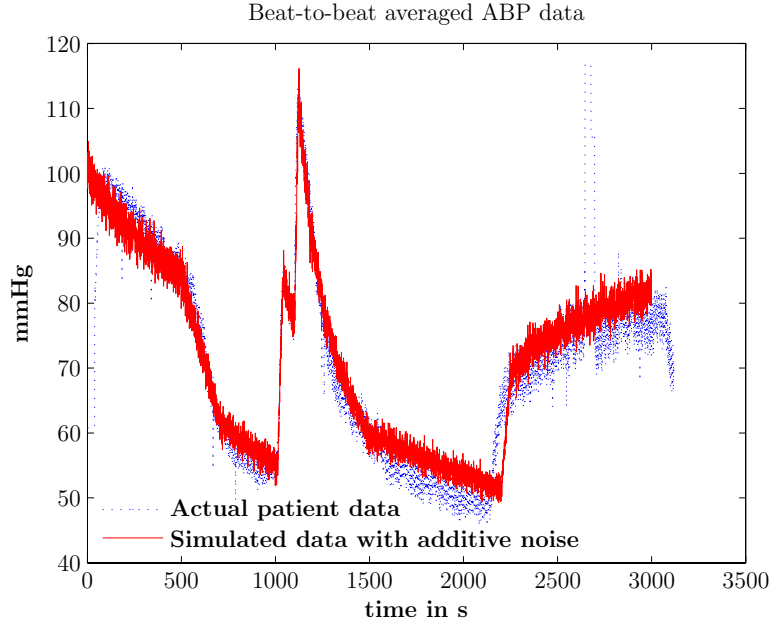


Figure 5-4: Beat-to-beat averaged ABP data: actual and simulated with additive noise.

Having matched the patient data, we assume knowledge of the initial patient state and we attempt to estimate and track certain parameters of physiological interest.

## 5.4 Parameter Tracking

As the bleeding rate and rate of change of  $R_a$  are responsible for the pathology of the patient, we track these two parameters in time. We assume that the initial patient state is known; this state includes the initial values of all the parameters and state variables<sup>2</sup>. To estimate and track the parameters in time, the pseudo-patient ABP data is divided into non-overlapping, 100s windows which are used to recover the two parameters using the Gauss-Newton nonlinear least squares estimation technique. In addition to estimating the two parameters of interest, the initial conditions for all the frames, except the initial one, need to be estimated. In order to estimate the initial conditions for the current frame, we

---

<sup>2</sup>For the start of the simulation, the initial state variables are determined by the initial parameter values using Equations 2.18 - 2.25.

run the model for the time duration of a frame using the parameter estimates and initial conditions of the previous frame. The end-diastolic<sup>3</sup> conditions for the last beat in this simulation are then used as initial conditions for the current frame. As the fluid boluses administered are assumed to be known quantities, the volume changes are accounted for when estimating the parameters during the times of fluid resuscitation.

First, we employed this algorithm on noise-free pseudo-patient data so that any issues with the estimation formulation could be easily identified. We encountered two issues with this estimation scheme, which are elaborated on next.

**Choice of Observable Data** It turns out that bleeding rate and rate of change of  $R_a$  have similar effects on ABP data. In fact, the angle between the Jacobian columns corresponding to these two parameters is  $0.067\pi$  radians, indicating that they are almost collinear. Thus, using only ABP data for estimation leads to a degeneracy in the system, as the two parameter estimates can be distorted without affecting the error criterion. To overcome this problem, we assume that the pseudo-patient central-venous pressure (CVP) is also observable and can be used to estimate the parameters in conjunction with ABP data. Figure 5-5 illustrates the plot of the noise-free, pseudo-patient beat-to-beat averaged CVP data. Including the use of CVP for parameter recovery empowers the estimation algorithm with greater discerning ability, as the two parameters tend to affect ABP and CVP differently. For example, an increase in  $R_a$  near the end of the time-period causes ABP to increase, whereas CVP still decreases.

**Estimating the Initial Conditions** Under the scheme described to estimate initial conditions, the end-diastolic conditions of the last beat in the previous frame are used as initial conditions for the current frame. This method ignores the effects of the intra-beat dynamics that occur within the last beat of the previous frame. Though the intra-beat dynamics last for only a very short-period of time, ignoring their effects caused severe distortion in the parameter estimates. Moreover, as the parameter estimates for the current frame depend on

---

<sup>3</sup>The simulator expects initial conditions to be end-diastolic.

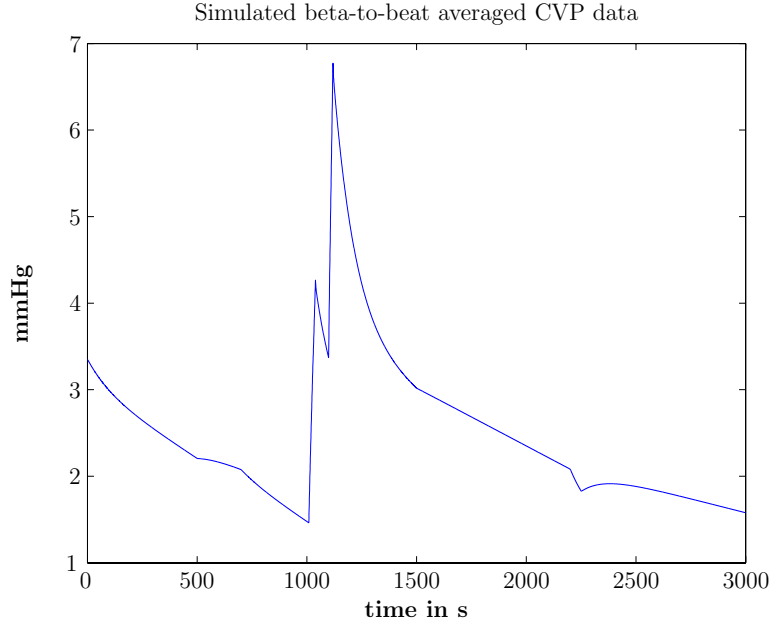


Figure 5-5: Simulated beat-to-beat averaged CVP data.

the estimates of the previous frame, any error incurred propagates and builds up.

Consider the frames during which fluid resuscitation takes place. Estimating a frame's initial conditions using the proposed methodology ignores the volume of fluid that is administered for the duration of a beat. Figure 5-6 illustrates this problem diagrammatically. Neglecting the volume administered within a beat leads to significant estimation errors, which build up in subsequent frames. Figure 5-7a shows a portion of data that corresponds to a frame that follows the end of fluid administration. The plot also shows the reconstruction of the same data portion using exact parameter values and estimated initial conditions which neglect the volume of fluid administered during the last beat of the previous frame. We observe that there is a mismatch between the data and its reconstruction, which causes the estimation algorithm to distort the parameters in an attempt to better match the pseudo-patient data.

To overcome this problem, we included ABP and CVP initial condition estimation in the nonlinear least squares problem, while the initial conditions for the rest of the state-variables were estimated as described before. Estimating the initial conditions of the observable

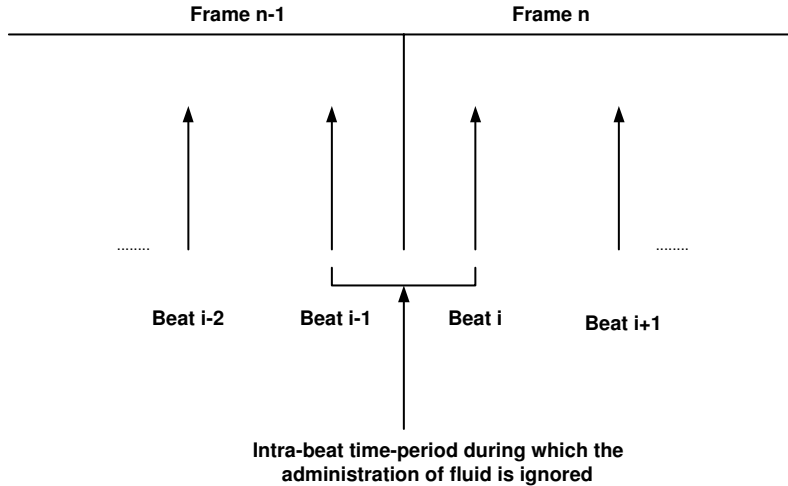


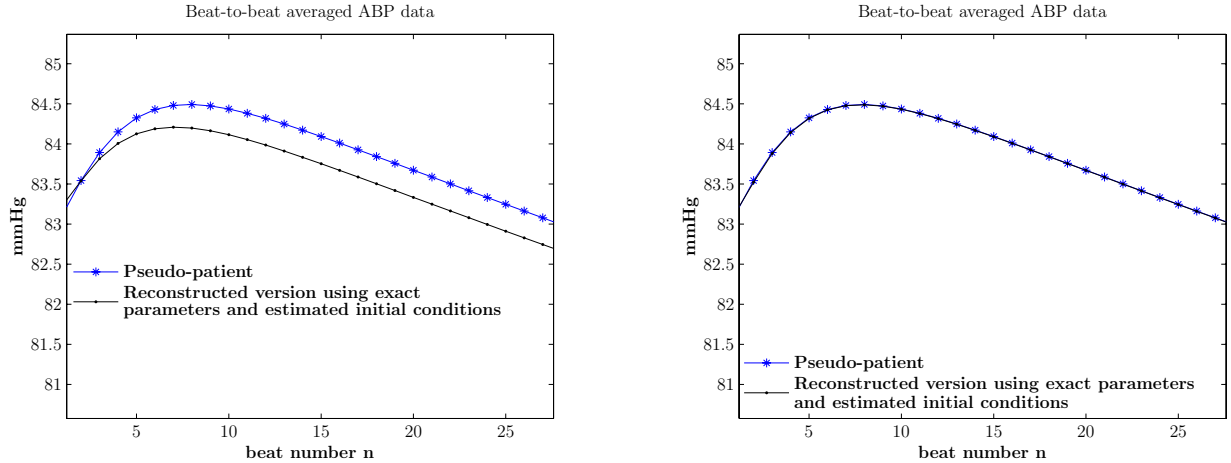
Figure 5-6: Diagram depicting the neglect of intra-beat dynamics under the proposed scheme to estimate initial conditions.

state-variables, instead of simply using previous beat values, allows for the incorporation of intra-beat dynamics to some extent. Figure 5-7b shows the same portion of data as Figure 5-7a, along with its reconstructed version using exact parameter values and the estimated initial conditions using the updated scheme. We observe that the two plots are almost indistinguishable, indicating that the updated scheme performs better.

After updating our choice of observable output by including the use of CVP data for estimation, and after improving the method of estimating initial conditions by incorporating two of them in the nonlinear least squares formulation, we employed the estimation algorithm on noise-corrupted pseudo-patient data. We present the results of the estimation algorithm next.

## 5.5 Results

Figure 5-8 shows the plot of the estimated parameters versus the actual ones. The algorithm does a reasonably good job of recovering and tracking the bleeding rate and rate of change of  $R_a$ , with mean estimation error less than 6% for either case. In fact, the error distributions are statistically indistinguishable from a 0-mean distribution, with a significance level  $\alpha = 0.05$ .



(a) Estimating the initial conditions by running the simulation for the previous time-frame. (b) Estimating ABP and CVP initial conditions through nonlinear least squares.

Figure 5-7: Plot showing portion of ABP data following a fluid bolus and its reconstructed version using exact parameters and estimated initial conditions using two different schemes.

This implies that for either case, the interval that contains the true mean of the error distribution with probability  $1 - \alpha$  (0.95) includes the 0 value.

## 5.6 Concluding Remarks

In this chapter, we investigated the viability of temporally tracking selected model parameters of physiological interest, assuming knowledge of initial values of the parameters. We used synthetic data that was representative of a real case of hemorrhage to track bleeding rate and rate of change of  $R_a$ . Our simulations show promising results for dynamically tracking selected parameters of interest. This can be of great value to patient monitoring, as the time evolution of these parameters would reveal information about disease progression.

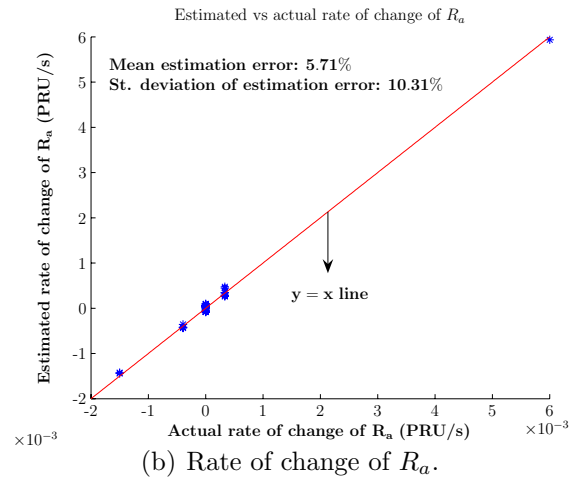
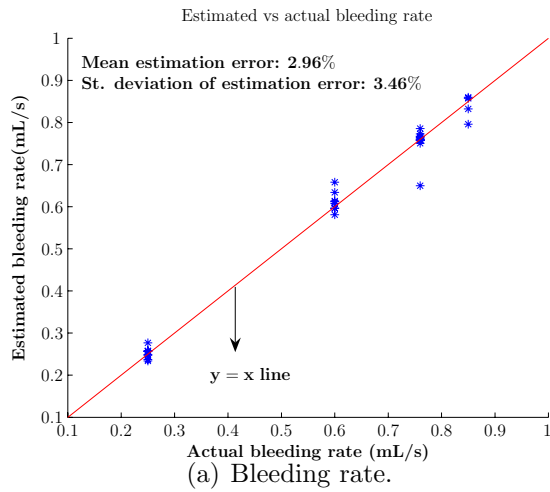


Figure 5-8: Estimated versus actual parameters.

# Chapter 6

## Conclusions and Recommendations for Future Work

In this thesis, we explored model-based quantitative methods of estimating selected cardiovascular parameters over time. Tracking the time evolution of the parameters could reveal information about disease progression and hence can be very useful for patient monitoring purposes. Our effort was divided into two parts: constructing a computational model, and using it for investigating parameter estimation techniques.

In this chapter, we summarize our efforts and results, after which we suggest directions for future work.

### 6.1 Summary

In Chapter 2, we outlined and detailed the implementation of a pulsatile cardiovascular model based on Davis's CVSIM model [4]. We built the model in Simulink, which is a strong tool for implementing dynamic systems. The abstractions provided by the building-blocks, and the built-in functions and routines, make the reliable extension of the model relatively simple, which is of great value in simulating various disease conditions. Furthermore, we enhanced the functionality of the CVSIM model by adding an interstitial fluid compartment. The role

of the interstitial compartment becomes significant during transients resulting from disease conditions or clinical interventions that cause volume shifts between the intravascular and interstitial spaces. Our model implementation was validated based on analysis of the intra- and inter-cycle dynamics.

In Chapter 3, we described the implementation of the arterial baroreflex, which is a principal component of short-term, neurally mediated control. Our implementation of the control system was based on Davis’s extension of deBoer’s work [4, 23]. The arterial baroreflex is modeled as a set-point controller that senses the blood pressure and responds to the error signal, which is the deviation of the sensed pressure from the set-point. In order to reduce the error signal, the arterial baroreflex controls sympathetic and parasympathetic activity, which in turn affects zero-pressure venous volume, heart rate, ventricular contractility, and peripheral resistance. Previous implementations of the arterial baroreflex used relatively coarse time-steps for the control system as compared to the rest of the model. However, as such implementations lead to aliasing effects, we implemented the control system in continuous-time (to be handled numerically along with other continuous-time components). Furthermore, as parasympathetic dynamics last for only a fraction of a heart beat, they do not significantly affect the model output; we therefore simplified the parasympathetic block implementation to a simple gain. Our implementation of the short-term control system was qualitatively validated based on responses to simulated conditions of hemorrhage and myocardial infarction.

In Chapter 4, we turned our attention to parameter estimation. We used a nonlinear least squares optimization technique to estimate cardiovascular parameters based on waveform data that is continuously available in an ICU setting. We highlighted the problem associated with an ill-conditioned Hessian matrix and subsequently outlined the subset-selection algorithm that improves the Hessian conditioning by reducing the dimensionality of the estimation problem. The subset selection algorithm identifies a subset of parameters that can be estimated robustly, while the rest are fixed at their nominal values. Our simulations show promising results for estimating well-conditioned parameters using both

steady-state and transient data.

In Chapter 5, we explored the viability of tracking selected parameters of physiological interest using beat-to-beat averaged data, assuming prior knowledge of initial parameter values. Our investigation was based on a real patient hemorrhage case, and involved tracking the bleeding rate and rate of change of peripheral resistance. As the patient data available was not sufficient to determine the actual parameter values, we used our model to match the patient data, and then we used the simulated data for estimation so that the performance of the estimation algorithm could be judged quantitatively. The results of Chapter 5 are encouraging, as we were able to track successfully the two parameters of physiological significance.

## 6.2 Recommendations for Future Work

In conducting our research efforts, we identified the following directions for further work:

**Parameter Estimation** In Chapter 4, our optimization technique was constrained to use the entire single-cycle waveforms of ABP, CVP, and PAP to estimate the cardiovascular parameters. We followed a ‘*more is better*’ approach and did not analyze the structure of the Jacobian to determine if some signals, or sections thereof, are more suitable to recover certain parameters over others. Further investigation needs to be conducted on the relationship between quality of parameter estimates and the number, type, and section (e.g., systolic or diastolic) of signals used for estimation.

So far we have only applied the estimation algorithms on synthetic data, as real patient data with a sufficient number of observable signals and well annotated by a doctor or surgeon, was not available. To validate the reliability of the algorithms, it is necessary to apply them on real data. In order to do so, we need patient data with ABP, CVP, and PAP waveform recordings. Supplementary recordings, such as cardiac output, would be helpful, as they would play a role in judging the quality of some of the estimates.

**Estimating the Initial Values of the Parameters** In Chapter 5, we assumed knowledge of the initial values of the parameters and we tracked two of the physiologically relevant ones using ABP and CVP signals that are continuously available in an ICU setting. In estimating the initial values of the parameters, however, we are not limited by the data streams that are available constantly - we can use all the available data, including cardiac output, left-ventricular end-diastolic pressure, imaging studies, etc., to estimate the initial values. Zhao developed a set of heuristic algorithms that used steady-state data to estimate the parameters [16]. Further investigation should focus on developing quantitative methods that use all available information to determine the initial values of the parameters in transient conditions.

**Cycle-Averaged Models** Transients spanning long periods of time are sufficiently represented by trend data, which includes beat-to-beat averages. In such cases, the high-resolution waveform data is not necessary for analysis. We would expect the models that ignore the fine intra-beat dynamics and produce only cycle-averages to be more computationally efficient and relatively simple in structure as compared to the pulsatile models. Such models could be very useful in inverse-modeling studies, where the simplicity in their structure can be exploited to recover the underlying parameters. Development of cycle-averaged models is a subject of ongoing research in our group. Simple cycle-averaged models consisting of a single heart chamber, which consider the time-varying ventricular elastance function to be either a step function, or a piecewise linear function, have already been developed [29, 30]. Current focus is now on extending the cycle-averaged model to include two heart chambers and a control system.

**Knowledge-Based Systems** Algorithms that estimate cardiovascular parameters using real patient data need to be integrated with knowledge-based systems to enhance their robustness and reliability and to aid in patient monitoring. The knowledge-based systems can be trained to interpret the physiological significance of parameter values, and using the estimates, they can help in generating hypotheses regarding patient state, track patient

trajectory, and generate alarms based on physiologically significant events.



# Appendix A

## Updated CVSIM Model Equations

Figure A-1 shows the circuit analog of the updated CVSIM model with the interstitial compartment. Applying Kirchhoff's Current Law (KCL) to the circuit topology of the model, the following set of equations is obtained:

$$\frac{dP_l}{dt} = \frac{\dot{q}_{li} - \dot{q}_{lo} - (P_l - P_{th}) \cdot dC_l(t)/dt}{C_l(t)} \quad (\text{A.1})$$

$$\frac{dP_a}{dt} = \frac{\dot{q}_{lo} - \dot{q}_a}{C_a} \quad (\text{A.2})$$

$$\frac{dP_v}{dt} = \frac{\dot{q}_a - \dot{q}_{int} - \dot{q}_{ri}}{C_v} \quad (\text{A.3})$$

$$\frac{dP_{int}}{dt} = \frac{\dot{q}_{int}}{C_{int}} \quad (\text{A.4})$$

$$\frac{dP_r}{dt} = \frac{\dot{q}_{ri} - \dot{q}_{ro} - (P_r - P_{th}) \cdot dC_r(t)/dt}{C_r(t)} \quad (\text{A.5})$$

$$\frac{dP_{pa}}{dt} = \frac{\dot{q}_{ro} - \dot{q}_{pa}}{C_{pa}} \quad (\text{A.6})$$

$$\frac{dP_{pv}}{dt} = \frac{\dot{q}_{pa} - \dot{q}_{li}}{C_{pv}} \quad (\text{A.7})$$

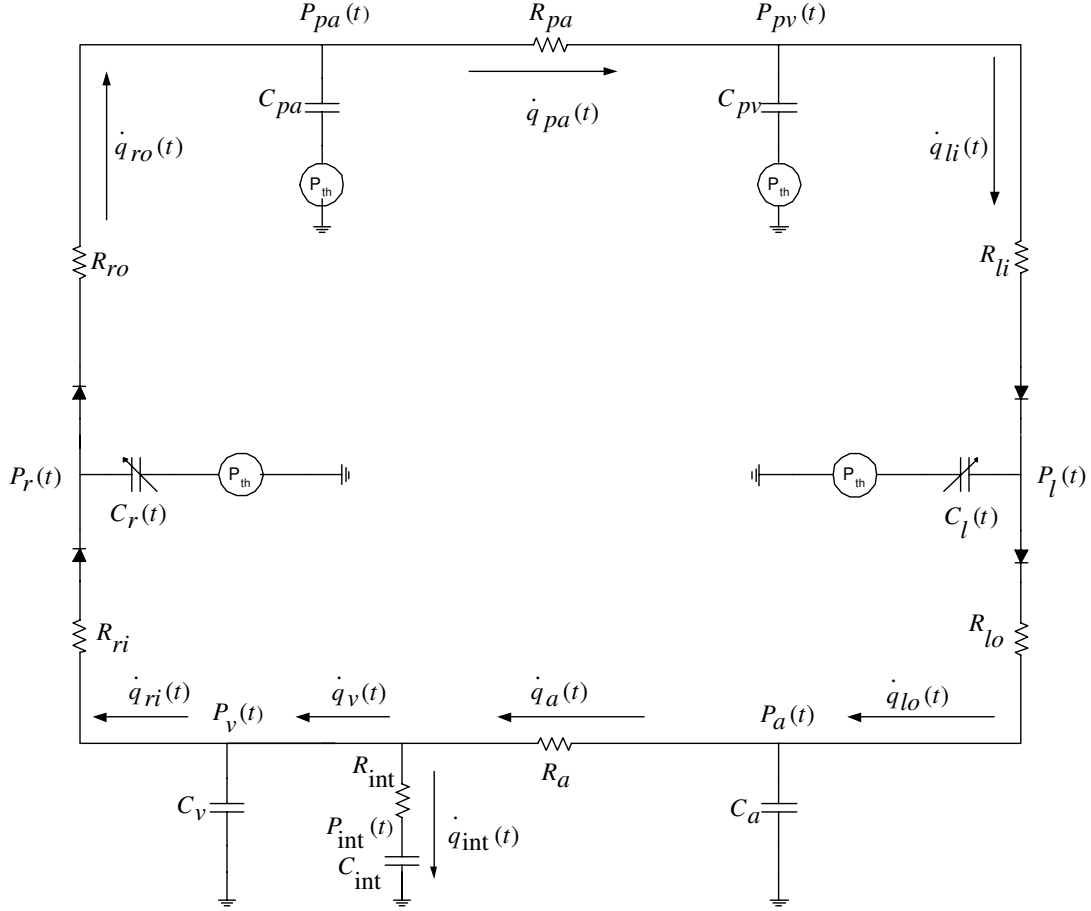


Figure A-1: Circuit analog of the updated CVSIM model.

The compartmental flow rates are obtained from the defining equation for resistors:

$$\dot{q}_{li} = \begin{cases} \frac{P_{pv} - P_l}{R_{li}} & \text{if } P_{pv} > P_l \\ 0 & \text{otherwise} \end{cases} \quad (\text{A.8})$$

$$\dot{q}_{lo} = \begin{cases} \frac{P_l - P_a}{R_{lo}} & \text{if } P_l > P_a \\ 0 & \text{otherwise} \end{cases} \quad (\text{A.9})$$

$$\dot{q}_a = \frac{P_a - P_v}{R_a} \quad (\text{A.10})$$

$$\dot{q}_{int} = \frac{P_v - P_{int}}{R_{int}} \quad (\text{A.11})$$

$$\dot{q}_{ri} = \begin{cases} \frac{P_v - P_r}{R_{ri}} & \text{if } P_v > P_r \\ 0 & \text{otherwise} \end{cases} \quad (\text{A.12})$$

$$\dot{q}_{ro} = \begin{cases} \frac{P_r - P_{pa}}{R_{ro}} & \text{if } P_r > P_{pa} \\ 0 & \text{otherwise} \end{cases} \quad (\text{A.13})$$

The initial conditions for all the compartments except the interstitial compartment are calculated using Equations 2.18 - 2.25. As no net exchange of volume takes place between the intravascular and the interstitial spaces in steady-state, the initial interstitial compartment pressure is set equal to the initial venous pressure.



# Appendix B

## Independent Parameters of the CVSIM Model

Table B.1: Independent Parameters of the CVSIM Model (adapted from Heldt [7]).

<b>Description</b>	<b>Symbol</b>	<b>Unit</b>	<b>Value</b>
Left end-systolic elastance	$E_l^{es}$	$\frac{mmHg}{mL}$	$2.5 \pm 0.6$
Left end-diastolic elastance	$E_l^{ed}$	$\frac{mmHg}{mL}$	$0.1 \pm 0.015$
Right end-systolic elastance	$E_r^{es}$	$\frac{mmHg}{mL}$	$0.83 \pm 0.51$
Right end-diastolic elastance	$E_r^{ed}$	$\frac{mmHg}{mL}$	$0.1 \pm 0.043$
Left inflow resistance	$R_{li}$	PRU	$0.01 \pm 0.005$
Left outflow resistance	$R_{lo}$	PRU	$0.006 \pm 0.0017$
Right inflow resistance	$R_{ri}$	PRU	$0.01 \pm 0.005$
Right outflow resistance	$R_{ro}$	PRU	$0.003 \pm 0.0015$
Peripheral resistance	$R_a$	PRU	$1.0 \pm 0.3$
Pulmonary venous resistance	$R_{pv}$	PRU	$0.08 \pm 0.0457$
Arterial compliance	$C_a$	$\frac{mL}{mmHg}$	$1.6 \pm 0.3$
Venous compliance	$C_v$	$\frac{mL}{mmHg}$	$100 \pm 15$
Pulmonary venous compliance	$C_{pv}$	$\frac{mL}{mmHg}$	$8.4 \pm 2.8$
Pulmonary arterial compliance	$C_{pa}$	$\frac{mL}{mmHg}$	$4.3 \pm 1.77$
Distending blood volume	DBV	$mL$	$1175 \pm 138$

# Appendix C

## Peripheral Resistance Estimation based on Patient Data

In simulating the patient data in Chapter 5, we made certain assumptions regarding how peripheral resistance ( $R_a$ ) changes based on the ABP patient data and based on recorded changes in doses of Levophed. In this section, we use the Windkessel model [31, 32] of arterial dynamics to estimate  $R_a$  using the patient ABP data, in an attempt to validate our assumptions a posteriori.

### C.1 Assumptions on Changes in Peripheral Resistance

Figure C-1 shows a time-series plot of the patient beat-to-beat averaged ABP data and of the Levophed medication. Based on this information, we made the following assumptions regarding changes in  $R_a$ :

- At 500s, we assumed  $R_a$  starts to drop as it is preceded by a recorded reduction in Levophed dose, the effect of which is observed when the patient's ABP drops soon after. We continued to reduce  $R_a$  till 700s when ABP stopped to drop as rapidly as before.
- As the patient's ABP drops rapidly starting at 1120s, with a subsequent recorded

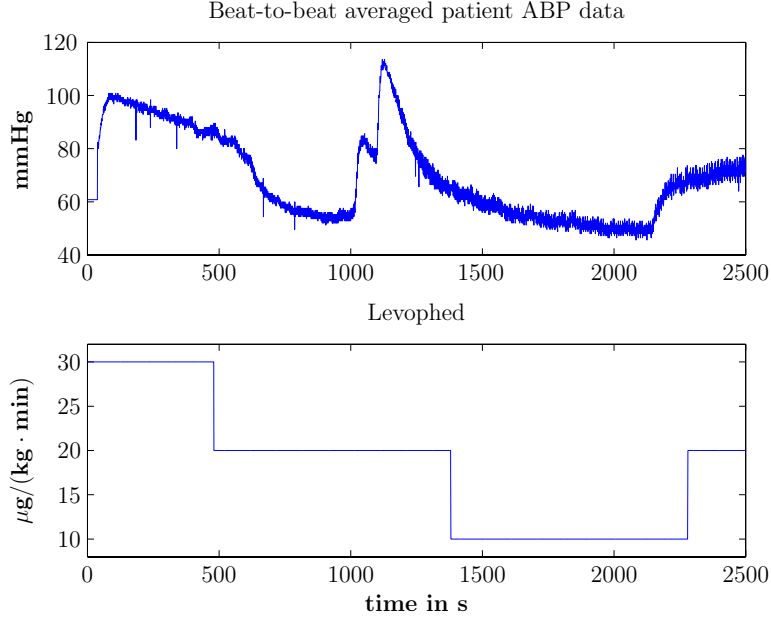


Figure C-1: Beat-to-beat averaged patient ABP data (top panel) and Levophed medication (bottom panel).

reduction in Levophed dose, we hypothesized a further drop in  $R_a$  starting at 1120s and ending at 1500s. The discrepancy between the time ABP starts to drop and the recorded time at which the Levophed dose changes can be attributed to a recording artifact.

- An increase in ABP starting at 2200s and a subsequent increase in Levophed dose led us to hypothesize an increase in  $R_a$  starting at 2200s. The time difference between the Levophed dose change and the point at which ABP starts to increase can again be attributed to a recording artifact.

## C.2 Peripheral Resistance Estimation using the Windkessel Model

The Windkessel model is a simple three-element circuit model of arterial dynamics [31, 32]. Figure C-2 shows the circuit analog of the Windkessel model. The current source,

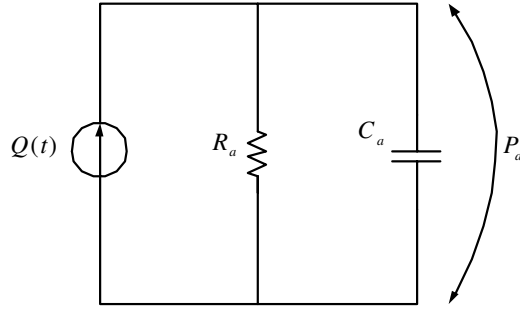


Figure C-2: Circuit analog of Windkessel model.  $P_a$  refers to arterial blood pressure.

which drives the circuit with impulses, represents the pumping heart, ejecting blood into the circulation instantaneously. The resistor represents the peripheral resistance whereas the capacitance models the arterial compliance ( $C_a$ ).

Through the application of circuit theory, it can be shown that stroke-volume is proportional to pulse pressure ( $PP$ ), with the constant of proportionality being the arterial compliance. Pulse pressure is defined as the difference between systolic and diastolic arterial pressures. In electrical circuit terms,  $\Delta Q = C_a \cdot \Delta V$ , with  $\Delta Q$  being analogous to stroke-volume and  $\Delta V$  being analogous to pulse pressure.

The blood pressure data can therefore be used to calculate  $R_a$  in the following manner:

$$R_a = 60 \cdot \frac{\overline{ABP}}{PP * HR * C_a}$$

where  $\overline{ABP}$  refers to beat-to-beat averaged ABP and HR represents the heart rate. A quantity proportional to  $R_a$  can be obtained, as  $C_a$  is constant in the Windkessel model:

$$R_a \sim 60 \cdot \frac{\overline{ABP}}{PP * HR}$$

This quantity can be used as a relative estimate of  $R_a$ , which we shall refer to as the Windkessel estimate.

Figure C-3 shows a plot of the Windkessel  $R_a$  estimate using the patient ABP data. The plots of the patient ABP data and Levophed medication are also shown. The Windkessel

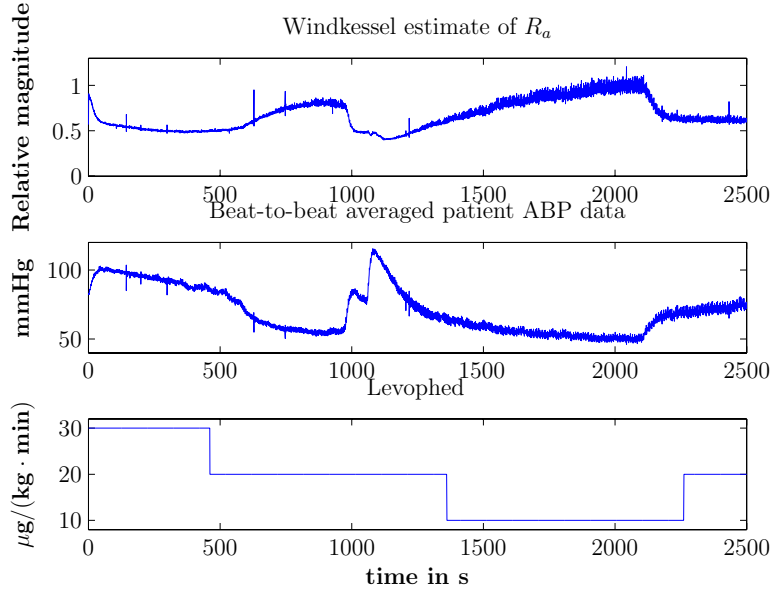


Figure C-3: Windkessel estimate of  $R_a$  (top panel), beat-to-beat averaged patient ABP data (middle panel), and Levophed medication (bottom panel).

$R_a$  estimate behaves exactly *opposite* to our intuition. Whenever ABP decreases, along with the Levophed dose, the Windkessel estimate of  $R_a$  increases and vice-versa. One possible explanation for this behavior is the intervention by the control system. Whenever ABP decreases, the control system intervenes to increase ABP and therefore increases  $R_a$ . However, it must also be taken into account that the derived estimate of  $R_a$  assumed a constant  $C_a$ , whereas physiologically,  $C_a$  exhibits a nonlinear volume-pressure relationship [33].

Based on an arctangent model of aortic mechanics, Langewouters and co-workers [34] proposed a method of calculating  $C_a$  that incorporates the nonlinear behavior:

$$C_a = \frac{A_{max}/\pi P_1}{1 + \left(\frac{P_a - P_0}{P_1}\right)^2} \quad (\text{C.1})$$

Here  $P_a$  refers to arterial blood pressure;  $A_{max}$ ,  $P_0$ , and  $P_1$  are constants denoting the maximum thoracic aortic cross-sectional area, inflection point of pressure, and width-parameter respectively, and are derived from aortic pressure-area relationships. Through population

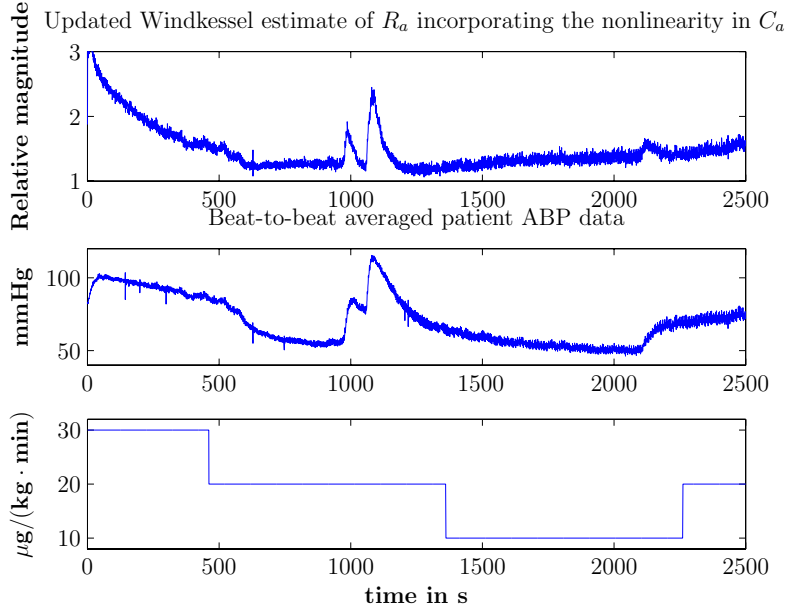


Figure C-4: Windkessel estimate of  $R_a$  incorporating the nonlinearity in  $C_a$  (top panel), beat-to-beat averaged patient ABP data (middle panel) and Levophed medication (bottom panel).

studies, Wesseling and co-workers [35] determined the values of these constants based on gender and age. We applied Equation C.1 to our patient data to obtain a  $C_a$  that varies nonlinearly with ABP<sup>1</sup>. The calculated  $C_a$  was then incorporated into the Windkessel model to obtain the updated Windkessel  $R_a$  estimate that takes the  $C_a$  nonlinearity into account.

Figure C-4 shows the updated Windkessel  $R_a$  estimate. The updated estimate overlaps to some degree with our assumptions. The decrease in  $R_a$  that we assumed from 500 – 700s is present in the updated estimate, and so is the increase in  $R_a$  that we assumed from 2200s onwards. However, the starting points of these changes are not aligned with our assumptions. We hypothesized a decrease in  $R_a$  from 500s, whereas in the updated estimate  $R_a$  decreases from the start. A similar starting-point mismatch is observed for the increase in  $R_a$  that we assumed started at 2200s. Moreover, the updated estimate shows an increase in  $R_a$  during the times of bolus administration. We are not quite sure why the estimate is showing an

<sup>1</sup>The calculation of the nonlinear  $C_a$  was provided to us courtesy James Sun, who also introduced us to the work of Langewouters and Wesseling [34, 35].

increase in  $R_a$  in that region. Ignoring the region of bolus administration and the subsequent recorded drop in Levophed dose, and assuming long time-lags exist to record the changes in medication, we can somewhat correlate the changes in the updated  $R_a$  estimate to the Levophed medication. The decrease in the estimated  $R_a$  from the start can be caused by the decrease in Levophed dose which is recorded at approximately 500s. Similarly, the increase in  $R_a$  which starts at approximately 1300s can be related to the increase in Levophed dose which is recorded at approximately 2250s. However, this lag of more than 15 minutes is slightly long to be attributed to a recording artifact, but it is possible.

### C.3 Concluding Remarks

In this section, we used the Windkessel model to estimate  $R_a$  for the patient case we considered in Chapter 5. The idea was to use a simple arterial side model to estimate  $R_a$  using actual patient data, in an attempt to validate the assumptions we made when simulating the patient. The Windkessel  $R_a$  estimate turned out to exhibit exactly the opposite behavior to our assumptions. However, the Windkessel estimate itself is not very reliable as it makes several simplifying assumptions including instantaneous ejection and a constant  $C_a$ . To incorporate the nonlinear  $C_a$  into the Windkessel estimate, we used a method proposed by Langewouters and co-workers [34]. The updated  $R_a$  estimate had some overlap with our assumptions and was seen to be somewhat correlated to the changes in Levophed medication. However, the updated estimate did exhibit some inexplicable behavior in the region of bolus administration.

The analysis performed in this section serves to show the difficulty in estimating  $R_a$  using only ABP data. Given only ABP data, we are limited to using simple arterial side models that make several simplifying assumptions and ignore important components with which the arterial side interacts, such as the venous compartment. Thus, such models are not very representative of the underlying physiology, and can lead to misleading results. One simple solution to this problem is increased use of cardiac output recordings in the ICU setting, which can be used to calculate  $R_a$ .

# Bibliography

- [1] Exercise Physiology Digital Image Archive - Overview of the Cardiovascular System. <http://www.abacon.com/dia/exphys/five.html>.
- [2] A. Guyton and J. Hall. *Textbook of Medical Physiology*. W.B. Saunders, Philadelphia, 10th edition, 2000.
- [3] R.D. Berger, J.P. Saul, and R.J. Cohen. Transfer function analysis of autonomic regulation I. Canine atrial rate response. *American Journal of Physiology*, 256(25):H142–H152, 1989.
- [4] T. Davis. Teaching Physiology Through Interactive Simulation of Hemodynamics. Master’s thesis, Department of Electrical Engineering and Computer Science, Massachusetts Institute of Technology, Cambridge, MA, February 1991.
- [5] R.W. Milnor. Normal circulatory function. In V.B. Mountcastle, editor, *Medical Physiology*, chapter 37, pages 930–943. Mosby, 13th edition, 1974.
- [6] R.W. Milnor. The pulmonary circulation. In V.B. Mountcastle, editor, *Medical Physiology*, chapter 42. Mosby, 13th edition, 1974.
- [7] T. Heldt. *Computational Models of Cardiovascular Response to Orthostatic Stress*. PhD thesis, Harvard-MIT division of Health Sciences and Technology, Massachusetts Institute of Technology, Cambridge, MA, September 2004.
- [8] C. Perrow. *Normal Accidents*. Basic Books, Inc., New York, 1984.

- [9] S. Lawless. Crying wolf: False alarms in a pediatric ICU. *Critical Care Medicine*, 22:981–984, 1994.
- [10] Y. Donchin, D. Gopher, M. Olin, Y. Badihi, M. Biesky, C.L. Sprung, R. Pizov, and S. Cotev. A look into the nature and causes of human errors in the intensive care unit. *Critical Care Medicine*, 23:294–300, 1995.
- [11] A. Noordergraaf. Development of an analog computer for the human systemic circulatory system. In A. Noordergraaf, G.N. Jager, and N. Westerhof, editors, *Circulatory Analog Computers*. North-Holland Publishing Company, Amsterdam, 1963.
- [12] A.C. Guyton, T.G. Coleman, and H.J. Granger. Circulation: Overall regulation. *Annual Review of Physiology*, 34:13–46, 1972.
- [13] M. Guarini, J. Urzúa, A. Cipriano, and W. González. Estimation of cardiac function from computer analysis of the arterial pressure waveform. *IEEE Transactions on Biomedical Engineering*, 45(12):1420–1428, December 1998.
- [14] P. Molino, C. Cerutti, C. Julien, G. Cuisinaud, M. Gustin, and C. Paultre. Beat-to-beat estimation of windkessel model parameters in conscious rats. *American Journal of Physiology - Heart and Circulatory Physiology*, 274:171–177, 1998.
- [15] Burattini R., G. Gnudi, N. Westerhof, and S. Fioretti. Total systemic arterial compliance and aortic characteristic impedance in the dog as a function of pressure: a model-based study. *Computers and Biomedical Research*, 20:154–165, 1987.
- [16] R. Zhao. A Model-Based Expert System for Interpretation of Hemodynamic Data from ICU Patients. Master’s thesis, Department of Electrical Engineering and Computer Science, Massachusetts Institute of Technology, Cambridge, MA, May 1997.
- [17] K. Muralidhar. Central venous pressure and pulmonary capillary wedge pressure monitoring. *Indian Journal of Anaesthesia*, 46(4):298–303, 2002.

- [18] R. Mukkamala. *A Forward Model-Based Analysis of Cardiovascular System Identification Methods*. PhD thesis, Department of Electrical Engineering and Computer Science, Massachusetts Institute of Technology, Cambridge, MA, June 2000.
- [19] H. Suga and K. Sagawa. Instantaneous pressure-volume relationships and their ratio in the excised, supported canine left ventricle. *Circulation Research*, 35:117–126, 1974.
- [20] H. Suga, K. Sagawa, and A.A. Shoukas. Load independence of the instantaneous pressure-volume ratio of the canine left ventricle and effects of epinephrine and heart rate on the ratio. *Circulation Research*, 32:314–322, 1973.
- [21] W.H. Press, S.A. Teukolsky, W.T. Vetterling, and B.P. Flannery. *Numerical Recipes in C - The Art of Scientific Computing*. Cambridge University Press, New-York, 2nd edition, 1995.
- [22] M. Korula. Fluid and Blood Therapy in Trauma, January 2003. <http://www.theiaforum.org/january2003.htm>.
- [23] R.W. DeBoer, J.M. Karemaker, and J. Stackee. Hemodynamic fluctuations and baroreflex sensitivity in humans: A beat-to-beat model. *American Journal of Physiology - Heart and Circulatory Physiology*, 253(22):H680–H689, 1987.
- [24] G. Mancina and A.L. Mark. Arterial baroreflexes in humans. In *Handbook of Physiology, Section 2: The Cardiovascular System, Vol. III*, Part 3, pages 755–793. Bethesda, MD, 1983. American Physiological Society.
- [25] Y. Bard. *Nonlinear Parameter Estimation*. Academic Press, New York, 1974.
- [26] M. Burth, G.C. Verghese, and M. Vélez-Reyes. Subset selection for improved parameter estimation in on-line identification of a synchronous generator. *IEEE Transactions on Power Systems*, 14(1):218–225, 1999.

- [27] Vélez-Reyez M. *Decomposed Algorithms for Parameter Estimation*. PhD thesis, Department of Electrical Engineering and Computer Science, Massachusetts Institute of Technology, Cambridge, MA, September 1992.
- [28] G.H. Golub, V. Klema, and G.W. Stewart. Rank degeneracy and least squares problems. Technical Report TR-456. Department of Computer Science, University of Maryland, College Park, MD, 1976.
- [29] T. Heldt, J.L. Chang, G.C. Verghese, and R.G. Mark. Cycle-averaged models of cardiovascular dynamics. In D.D. Feng and E.R. Carson, editors, *Modelling and Control in Biomedical Systems 2003*, pages 387–391. Oxford, UK, 2003. International Federation of Autonomic Control, Pergamon.
- [30] T. Parlikar and G.C. Verghese. A Simple Cycle Averaged Model for Cardiovascular Dynamics. Submitted to the 27th IEEE EMBS Annual International Conference in Shanghai, September 2005.
- [31] O. Frank. Schätzung des Schlagvolumens des menschlichen Herzens auf Grund der Wellen-und Windkesseltheorie. *Zeitschrift für Biologie*, 90:405–409, 1930.
- [32] O. Frank. Die Grundform des arteriellen Pulses. Erste Abhandlung. Mathematische Analyse. *Zeitschrift für Biologie*, 37:485–526, 1899.
- [33] R.M. Berne and M.N. Levy. *Cardiovascular Physiology*. Mosby-Year Book Inc., St. Louis, MI, 7th edition, 1997.
- [34] G.J. Langewouters, K.H. Wesseling, and W.J. Goedhard. The static elastic properties of 45 human thoracic and 20 abdominal aortas in vitro and the parameters of a new model. *Journal of Biomechanics*, 17(6):425–35, 1984.
- [35] K.H. Wesseling, J.R.C. Jansen, J.J. Settels, and J.J. Schreuder. Computation of aortic flow from pressure in humans using a nonlinear, three-element model. *Journal of Applied Physiology*, 74(5):2566–73, 1993.